

# Seasonal, latitudinal, and longitudinal trends in night-time ozone vertical structure on Mars from MAVEN/IUVS stellar occultations

Ashwin Braude, Franck Montmessin, Nicholas M. Schneider, Sumedha Gupta, Sonal K. Jain, Franck Lefèvre, Anni Määttänen, Loïc Verdier, Zachary Flimon, F. Jiang, et al.

▶ **To cite this version:**

Ashwin Braude, Franck Montmessin, Nicholas M. Schneider, Sumedha Gupta, Sonal K. Jain, et al.. Seasonal, latitudinal, and longitudinal trends in night-time ozone vertical structure on Mars from MAVEN/IUVS stellar occultations. Journal of Geophysical Research. Planets, 2023, 128 (5), pp.e2022JE007697. 10.1029/2022JE007697 . insu-04087186

**HAL Id: insu-04087186**
**https://insu.hal.science/insu-04087186**

Submitted on 23 May 2023

**HAL** is a multi-disciplinary open access archive for the deposit and dissemination of scientific research documents, whether they are published or not. The documents may come from teaching and research institutions in France or abroad, or from public or private research centers.

L'archive ouverte pluridisciplinaire **HAL**, est destinée au dépôt et à la diffusion de documents scientifiques de niveau recherche, publiés ou non, émanant des établissements d'enseignement et de recherche français ou étrangers, des laboratoires publics ou privés.



Distributed under a Creative Commons Attribution - NoDerivatives 4.0 International License

Check for updates

JGR Planets

RESEARCH ARTICLE
10.1029/2022JE007697

**Key Points:**

- The first study is presented distinguishing zonal variations in vertical ozone structure on Mars from seasonal and meridional trends
- Ozone variability is mostly driven by seasonal changes in the tropics but by zonal circulation patterns at higher latitudes
- Persistent regional enhancements in mesospheric ozone are observed at equatorial latitudes during aphelion season

**Supporting Information:**

Supporting Information may be found in the online version of this article.

**Correspondence to:**

A. S. Braude,
ashwin.s.braude@jpl.nasa.gov

**Citation:**

Braude, A. S., Montmessin, F., Schneider, N. M., Gupta, S., Jain, S. K., Lefèvre, F., et al. (2023). Seasonal, latitudinal, and longitudinal trends in nighttime ozone vertical structure on Mars from MAVEN/IUVS stellar occultations. *Journal of Geophysical Research: Planets*, *128*, e2022JE007697. https://doi.org/10.1029/2022JE007697

Received 30 NOV 2022
Accepted 24 APR 2023

© 2023 The Authors.
This is an open access article under the terms of the Creative Commons Attribution-NonCommercial License, which permits use, distribution and reproduction in any medium, provided the original work is properly cited and is not used for commercial purposes.

# Seasonal, Latitudinal, and Longitudinal Trends in Nighttime Ozone Vertical Structure on Mars From MAVEN/IUVS Stellar Occultations

**A. S. Braude[1], F. Montmessin[1], N. M. Schneider[2], S. Gupta[2], S. K. Jain[2], F. Lefèvre[1], A. Määttänen[1], L. Verdier[1], Z. Flimon[1,3], F. Y. Jiang[4], R. V. Yelle[4], J. Deighan[2], and S. M. Curry[5]**

[1]Laboratoire Atmosphères, Milieux, Observations Spatiales (LATMOS), UVSQ Université Paris-Saclay, Sorbonne Université, CNRS, Paris, France, [2]Laboratory for Atmospheric and Space Physics, University of Colorado Boulder, Boulder, CO, USA, [3]Royal Belgian Institute for Space Aeronomy (IASB-BIRA), Brussels, Belgium, [4]Lunar and Planetary Laboratory, University of Arizona, Tucson, AZ, USA, [5]Space Sciences Laboratory, University of California, Berkeley, Berkeley, CA, USA

**Abstract** Stellar occultation measurements conducted by the Mars Atmosphere and Volatile and EvolutioN/Imaging UltraViolet Spectrograph instrument were able to make vertically resolved measurements of ozone density in the middle atmosphere of Mars that offered good coverage with respect to latitude, longitude, and local time. These measurements were used to identify systematic variations in the vertical structure of ozone with longitude that could be distinguished from general trends in the evolution of ozone with respect to season and latitude. A total of 583 individual nightside occultations between Martian years 32 and 36 were analyzed, of which 224 were confirmed to have ozone, all found between $L_s$ = 15°–165°. Close to aphelion ($L_s$ = 60°–90°), peak ozone densities between 30 and 40 km altitude were observed to be within error of model predictions at all measured latitudes, but diverged from model predictions before and after this time. At low latitudes, seasonal changes were seen to have the greatest effect on the observed vertical structure of ozone, with detached ozone layer densities at altitudes above 30 km usually varying within approximately a factor of two along a given latitudinal band at a given time of year. Nonetheless, evidence of a persistent regional enhancement of ozone abundance was observed over equatorial latitudes during the aphelion season, spanning a longitude range of approximately 50°–130°E longitude. Planetary waves were clearly observed at higher Southern latitudes during Southern winter, often resulting in order of magnitude variations in ozone density with longitude.

**Plain Language Summary** The presence of ozone is key to the stability of carbon dioxide in the Martian atmosphere, and can also be used to monitor Martian meteorology. Previous measurements of vertical variations of ozone in the Martian atmosphere relied on orbiters designed mostly to look for latitudinal and seasonal trends in ozone on Mars, with little information on how ozone varies with longitude. We used data from the Imaging UltraViolet Spectrograph instrument on board the Mars Atmosphere and Volatile and EvolutioN orbiter to make independent measurements of seasonal, latitudinal, longitudinal, and altitudinal variations of ozone in the Martian atmosphere from March 2015 to January 2022. Close to the Equator of Mars, ozone tended to vary more with season than with longitude. Nonetheless, we observed a region of increased ozone densities in the Eastern hemisphere of Mars, centered over the Equator. This region was consistently seen during the same season of each observed Martian year. At higher latitudes, variations with longitude tended to be much larger and more important than seasonal variations. Variations in ozone also exhibited wave structures at Southern subpolar latitudes, possibly indicating meteorological patterns in the middle atmosphere of Mars.

## 1. Introduction

Ozone is produced in the Martian atmosphere when atomic oxygen (O), which forms from the photolysis of $CO_2$, recombines with molecular oxygen in the presence of $CO_2$ (the "three body reaction"). It is highly unstable to photolysis under the action of solar ultraviolet irradiation (Lefèvre & Krasnopolsky, 2017):

$$O + O_2 \xrightarrow{CO_2} O_3 \quad (1)$$

$$O_3 \xrightarrow{h\nu(\lambda>320nm)} O + O_2 \quad (2)$$

21699100, 2023, 5, Downloaded from https://agupubs.onlinelibrary.wiley.com/doi/10.1029/2022JE007697 by Cochrane France, Wiley Online Library on [23/05/2023]. See the Terms and Conditions (https://onlinelibrary.wiley.com/terms-and-conditions) on Wiley Online Library for rules of use; OA articles are governed by the applicable Creative Commons License

$$O_3 \xrightarrow{h\nu(\lambda<320nm)} O(^1D) + O_2(^1\Delta_g) \quad (3)$$

At the same time, the photolysis of water vapor in the Martian atmosphere is predicted to result in the formation of OH, H and, more indirectly, $HO_2$ radicals. These radicals are collectively referred to as $HO_x$, and inhibit the production of ozone through reaction with atomic oxygen:

$$O + HO_2 \rightarrow O_2 + OH \quad (4)$$

For this reason, ozone is predicted to be directly anticorrelated with water vapor in the Martian atmosphere (Clancy & Nair, 1996; Daerden et al., 2019).

OH radicals are also predicted to catalyze the recycling of CO back into $CO_2$ (McElroy & Donahue, 1972; Parkinson & Hunten, 1972), thereby preventing $CO_2$ from completely breaking down into CO in the upper atmosphere of Mars:

$$CO + OH \rightarrow CO_2 + H \quad (5)$$

Nonetheless, photochemical models (Lefèvre & Krasnopolsky, 2017; Lefèvre et al., 2021) based on our current understanding of $HO_x$ chemistry in the Martian atmosphere predict abundances of CO to be significantly lower than their observed values (e.g., Olsen et al., 2021). This is compounded by the difficulty in directly observing and constraining the abundances of $HO_x$ and $H_yO_x$ molecules on Mars, of which only hydrogen peroxide ($H_2O_2$) is confirmed to have been detected as of writing (Clancy et al., 2004; Encrenaz et al., 2004). On the other hand, ozone has a strong and broad absorption band centered around 255 nm (commonly referred to as the "Hartley band"), which has been frequently used to observe and study ozone in the Martian atmosphere since it was first detected there by the Mariner probes (Barth & Hord, 1971; Barth et al., 1973). Anticorrelations between ozone and water vapor, the main source of $HO_x$ in the Martian atmosphere, have been consistently confirmed by observation (e.g., Fast et al., 2006; Guslyakova et al., 2016; Lefèvre & Krasnopolsky, 2017; Olsen et al., 2022; Perrier et al., 2006 and references therein), albeit with some exceptions notably at low latitudes (Lefèvre et al., 2021). The presence of ozone can therefore be used to indirectly constrain the presence of $HO_x$ molecules which are otherwise difficult to detect in the Martian atmosphere. More broadly, the measurement of ozone allows for a better constraint on Martian atmospheric photochemistry, and to therefore better understand the stability of the $CO_2$ that makes up the bulk (~95%) of Mars' atmospheric composition. In addition, ozone may act as a tracer of dynamics, with a correlation between ozone and potential vorticity demonstrated by Holmes et al. (2017), and planetary waves around the polar vortex being inferred by measurements of the longitudinal distribution of near-surface ozone (Clancy et al., 2016).

Vertically integrated measurements of ozone column abundances (e.g., Clancy et al., 1999, 2016; Fast et al., 2006, 2009; Perrier et al., 2006; Willame et al., 2017) shed little light on how ozone density varies with altitude, but are thought to be dominated by a near-surface layer (<30 km altitude), where the comparatively high number density of $CO_2$ molecules allows for greater production of $O_3$ according to Equation 1. Although the first vertically resolved profiles of ozone abundance in the Martian atmosphere were retrieved by Mars 5 (Krasnopolsky & Parshev, 1979) and Phobos 2 (Blamont & Chassefiere, 1993; Blamont et al., 1989), they were confined to the day-night terminator and were limited in spatial and spectral coverage. Lebonnois et al. (2006) presented the first nightside vertical profiles of ozone, retrieved from the ultraviolet (UV) channel of the SPectroscopie pour l'Investigation des Caractéristiques Atmosphériques de Mars (SPICAM) instrument on board Mars Express. This was then followed by a comprehensive climatology of vertical ozone variation from the whole SPICAM data set in Määttänen et al. (2022a), combining both solar occultations (confined to the day/night terminators) and stellar occultations (mostly confined to the nightside hemisphere). These measurements were able to probe ozone at altitudes well above the surface of Mars, where ozone is produced through recombination during the night before being destroyed during the day by ultraviolet photolysis. A detached ozone layer forming over the Equator at around 30–50 km altitude was discovered from these results, together with another nighttime layer over the South Pole during winter at 50 km altitude (Lebonnois et al., 2006), later interpreted as resulting from large-scale summer-to-winter advection (Montmessin & Lefèvre, 2013). These layers form above the level of cloud condensation, where the presence of water vapor is diminished. Two instruments on board the ExoMars Trace Gas Orbiter mission (TGO, Vago et al. (2015), Korablev et al. (2018), and Vandaele et al. (2018)) then brought new independent measurements of vertical profiles of ozone. The Atmospheric Chemistry Suite (TGO/ACS)

21699100, 2023, 5, Downloaded from https://agupubs.onlinelibrary.wiley.com/doi/10.1029/2022JE007697 by Cochrane France, Wiley Online Library on [23/05/2023]. See the Terms and Conditions (https://onlinelibrary.wiley.com/terms-and-conditions) on Wiley Online Library for rules of use; OA articles are governed by the applicable Creative Commons License

instrument made the first observations of Martian ozone using weak absorption lines in the mid-infrared (Olsen et al., 2020, 2022), generally sensitive only to ozone below 30 km. The UV channel of the Nadir and Occultation for MArs Discovery (TGO/NOMAD) instrument made further climatologies of ozone using solar occultations in the mid-UV (Patel et al., 2021; Piccialli et al., 2023), including the first observation of a nighttime layer over the North winter pole (Daerden et al., 2022; Khayat et al., 2021).

Previous measurements of vertical variations of ozone in the UV using the occultation method have nonetheless been limited by the geometry of the orbiting probe, with TGO measurements in particular limited only to local sunrise and sunset. In addition, due to the instrumental designs of ACS, NOMAD, and SPICAM, only the general variability of ozone with respect to latitude and season could be explored. These measurements did not allow for zonal variability in ozone density to be reliably determined, that could either shed further light on distinct regional climatologies, or on short-term variability in local weather patterns that could cause perturbations in ozone density unrelated to general climactic trends. By contrast, UV stellar occultations from the Imaging Ultra-Violet Spectrograph (IUVS) instrument on board the Mars Atmosphere and Volatile and EvolutioN (MAVEN) orbiter (hereon referred to as MAVEN/IUVS, Jakosky et al., 2015; McClintock et al., 2015), allow for longitudinal variations in the vertical structure of ozone to be differentiated from latitudinal, seasonal and, to a lesser extent, diurnal variations in ozone. This is a capability that no other instrument to date has been able to provide. Gröller et al. (2018) presented a preliminary study on the general seasonal and latitudinal variability of ozone from a single Martian Year (MY) of MAVEN/IUVS data, going up to the end of MY 33 (March 2017). However, this data set was limited to 12 individual observation campaigns, of which only 70 stellar occultations spread over three observation campaigns were seen to have detectable amounts of ozone.

In this paper, we build on the work of Gröller et al. (2018) and expand it to a larger MAVEN/IUVS data set covering MY 32–MY 36 (March 2015–January 2022). We integrate an ozone detection limit procedure based on that of Teanby et al. (2009, 2019) with an existing retrieval pipeline (Gröller et al., 2018; Quémerais et al., 2006), in order to perform a comprehensive analysis of vertical, seasonal, and regional variations of ozone in the Martian atmosphere. We describe the IUVS stellar occultation data set in Section 2, and then illustrate our spectral and vertical inversion technique in Section 3, including a description of the selection method for determining significant ozone detections. In Section 4 we discuss general seasonal variations in our retrieved vertical ozone profiles over multiple latitudinal bands, and how they relate to longitudinal variations in ozone at different altitudes. Conclusions are presented in Section 5.

## 2. Data and Preprocessing

The IUVS instrument is a plane-grating spectrograph that has conducted stellar occultation observations of the Martian atmosphere since 2015. It makes use of a grating and a beam splitter that disperses incident solar radiation toward two diffraction orders: one covering the far-UV (FUV) between 110 and 190 nm, and the other covering the mid-UV (MUV) between 180 and 340 nm, at an approximate spectral resolution of 0.6 and 1.2 nm, respectively. Although IUVS is primarily designed to make measurements of the upper atmosphere of Mars (e.g., Chaffin et al., 2015; Clarke et al., 2017; Jain et al., 2015), it also has the capability of making measurements of the lower and middle atmosphere in occultation geometry, allowing for the simultaneous retrieval of profiles of $CO_2$, $O_2$, and $O_3$ density, together with aerosol (Gröller et al., 2018), at high vertical resolution. These measurements are conducted during brief campaigns which occur approximately once every two months lasting roughly 2 days each, and consist of 50–100 individual stellar occultations obtained over around 5 orbits (later increased to 12 orbits starting with Campaign 11 in November 2016). The spatio-temporal coverage of each of the campaigns carried out up to January 2022 is shown in Figure S1 in Supporting Information S1, with a single campaign shown as an example in Figure S2 in Supporting Information S1.

IUVS is mounted on an Articulated Payload Platform, which allows for more flexible pointings and orientations of the instrument relative to Mars or the Sun than was possible for SPICAM or the two instruments on board TGO. This means that stellar occultations could be conducted using a more targeted set of stars, and thereby maximize latitude and local time coverage for a given occultation campaign. For each selected star, a maximum of two sets of occultations (one at ingress and another at egress) could be carried out, with each of the occultations in the set located along a single latitudinal band and conducted at the same local time. In addition, the calibration procedure is essentially the same for all measurements carried out using the same star, thereby minimizing the impact of instrumental effects on variations in ozone density from occultation to occultation. Gröller

21699100, 2023, 5, Downloaded from https://agupubs.onlinelibrary.wiley.com/doi/10.1029/2022JE007697 by Cochrane France, Wiley Online Library on [23/05/2023]. See the Terms and Conditions (https://onlinelibrary.wiley.com/terms-and-conditions) on Wiley Online Library for rules of use; OA articles are governed by the applicable Creative Commons License

et al. (2018) previously showed that it was therefore possible to assume that any variation between individual occultations obtained using the same star was mostly due to genuine variation in atmospheric composition as a function of longitude, and not due to random instrumental effects. For every orbit completed by MAVEN around Mars, the central longitude of each occultation along a given latitudinal band initially advanced westwards by approximately 65° of longitude. In February 2019, an aerobraking campaign resulted in a lowering of the orbit of MAVEN around Mars, and hence a reduction in the orbital period of MAVEN from 4.5 to 3.5 hr, and a decrease in longitude sampling per orbit from 65° to 55°. The main disadvantage of the IUVS stellar occultation data, however, is the relatively sparse low solar longitude sampling (~20°–30° $L_s$) resulting from the infrequent nature of the occultation campaigns.

Calibration and straylight/background correction was carried out according to the procedure outlined in Gröller et al. (2018). It was at this stage that, of the 3,003 individual occultations in the total IUVS stellar occultation data set recorded to date, we decided to discard 2,382 occultations in this study that were seen to be unusable. Around 56% of the total data set, including all dayside observations and a significant proportion of nightside observations, had unsalvageable straylight contamination in the MUV due to sunlight scattered into the spectrometer by the Martian atmosphere. Other reasons for rejection of data included (a) the presence of airglow, (b) the absence of data from either the FUV or the MUV components, (c) straylight at long wavelengths (transmission at wavelengths longward of 280 nm > 1.1) that would have resulted in overestimated ozone number densities, or (d) the use of a star that was too faint to produce transmission spectra with an adequate signal-to-noise ratio (SNR). We therefore only made use of occultations that were conducted using the 40 brightest stars in our reference catalog (refer to Appendix A of Gröller et al. (2018)) ranked in descending order of ultraviolet flux, and also screened out occultations conducted using three stars (respectively $\alpha$ CMa, $\beta$ Ori, and $\alpha$ Gru) that were found to have a weak stellar signal in certain parts of the spectrum. A list of occultations analyzed following screening is given in Table S1.

Transmission spectra were then calculated through the division of the measured spectral radiances at each altitude with a reference spectrum obtained above 170 km, where negligible atmospheric absorption was seen in the data. Spectral uncertainties were calculated through the standard deviation of the time-varying signal at each wavelength from all spectra above 170 km, resulting in average SNR values in the MUV of approximately 30 for the brightest stars, but around 10 for more typical spectra. Spatio-temporal, geometrical, and altitudinal metadata associated with each occultation were derived from SPICE kernels as described in Gröller et al. (2018), with altitudes quoted with respect to the areoid. Throughout this analysis, we have defined longitudes east of the prime meridian.

## 3. Method

### 3.1. Spectral Inversion Procedure

In this work we made use of a two-step onion-peeling method to retrieve vertical gas profiles from the data, based mainly on the procedure of Gröller et al. (2018) with only a few modifications where explicitly stated. We initially retrieved independent values of column slant density at each altitude, assuming no vertical correlations between each of the individual spectra in a single occultation, based on the following forward model of the spectral transmission $T_{\lambda z}$ at each altitude $z$ (in km) as a function of wavelength $\lambda$ (in nm):

$$T_{\lambda z} = \sigma_{\mathrm{CO2}}(\lambda)X_{\mathrm{CO2}}(z) + \sigma_{\mathrm{O2}}(\lambda)X_{\mathrm{O2}}(z) + \sigma_{\mathrm{O3}}(\lambda)X_{\mathrm{O3}}(z) + \tau_z\left(\frac{250}{\lambda}\right)^{\alpha_z} \quad (6)$$

where $X_{\mathrm{gas}}(z)$ represents the vertical profiles of slant density (in units of $\mathrm{cm}^{-2}$) of each of the three gases in the model ($CO_2$, $O_2$, and $O_3$ respectively) as a function of altitude. The contribution of each gas to the total spectral absorption was modeled by a set of reference cross-section data $\sigma_{\mathrm{gas}}(\lambda)$, for which the full set of citations can be found in Table 2 of Gröller et al. (2018). The final term in the equation represents aerosol absorption modeled according to a simple power law, with $\tau_z$ being the aerosol optical depth normalized to a wavelength of 250 nm, and $\alpha_z$, a parameter which quantifies the gradient in transmission as a function of wavelength (the "Ångström coefficient"), and is dependent on particle size distribution (Dubovik et al., 2000; Montmessin et al., 2006; O'Neill & Royer, 1993). We did not correct for spectral shift in the inversion process as in Gröller et al. (2018), as the error in spectral shift correction was almost always negligible relative to the SNR and width of the Hartley band.

The individual profiles of $X_{\mathrm{gas}}(z)$, $\tau_z$, and $\alpha_z$ were initially all retrieved simultaneously using the MPFIT Levenberg-Marquardt optimal estimation algorithm (Markwardt, 2009). We started the retrieval process with the

21699100, 2023, 5, Downloaded from https://agupubs.onlinelibrary.wiley.com/doi/10.1029/2022JE007697 by Cochrane France, Wiley Online Library on [23/05/2023]. See the Terms and Conditions (https://onlinelibrary.wiley.com/terms-and-conditions) on Wiley Online Library for rules of use; OA articles are governed by the applicable Creative Commons License

spectrum obtained at the highest altitude at which there was reliable sensitivity to gaseous absorption, usually around 150 km, and then progressed downwards until the spectra at the lowest altitudes were reached. For each spectrum in the occultation, we initialized the a priori slant density values to those retrieved from the spectrum directly above in order to stabilize the retrieval and minimize unphysical vertical oscillations in slant density. Below around 80–100 km, the strong $CO_2$ absorption band starts to saturate around the wavelengths at which the main $O_2$ lines are located (around 110–180 nm), causing sensitivity to $O_2$ to be completely lost. We therefore fixed the volume mixing ratio of $O_2$ at $2 \times 10^{-3}$ for all altitudes below 80 km, where the contribution of $O_2$ absorption to the spectrum is essentially negligible. At the lowest altitudes (typically between around 10–20 km under the clearest atmospheric conditions), $CO_2$ and dust absorption becomes strong enough to render the atmosphere completely opaque at all wavelengths, making it impossible to retrieve ozone. We defined this lower altitude limit as the point at which $X_{CO2}(z)$ and $\tau_z$ could no longer be decoupled from each other, that is when the average SNR of the spectrum between 190 and 220 nm, where the combined absorption of $CO_2$ and $O_3$ is minimized, became equal to 1. For an occultation conducted using a typically bright star, this would generally occur when $\tau_z \gtrapprox 3$. The results of an example spectral fit to a single occultation, showing the main features of IUVS spectra within the approximate altitude range of sensitivity to ozone, are shown in Figure 1 for illustrative purposes.

Following spectral inversion, we excluded a further 38 occultations from the analysis that contained spectra which we predicted would have unphysically high values of ozone density following vertical inversion. This was determined by the following three-step procedure: (a) labeling stellar occultations as "problematic" if there was more than one spectrum in the occultation in which $\chi^2/n > 2.0$, for a total of $n$ wavelengths above 205 nm; (b) automatically screening out problematic occultations in which the phase angle of observation was greater than 105° (filtering out observations with excessive forward scattering of sunlight); and finally (c) screening the remainder of problematic occultations with phase angles below 105° on a case-by-case basis through qualitative visual inspection. This left a total of 583 useable occultations in the data set, for which the spatio-temporal distribution is shown in Figure 2. The number of occultations in each campaign before and after spectral inversion is given in Table S1.

### 3.2. Ozone Detection Limit Determination and Screening Procedure

A difficulty faced when retrieving ozone abundances from the Hartley band is that the uncertainties on those ozone abundances, as derived from error propagation in a Levenberg-Marquardt retrieval algorithm, do not always fully account for the presence of instrumental artifacts or other systematic sources of noise. These can cause distortions in the spectrum which, in limiting cases, can be mistaken for ozone by a retrieval code. It is therefore important to remove any false detections of ozone before attempting to retrieve local densities through vertical inversion, in order not to bias the vertical smoothing procedure with any erroneous values of ozone. Previous retrievals of ozone data (Gröller et al., 2018) using IUVS stellar occultations relied on subjective visual inspection to confirm the presence of ozone in individual spectra before filtering out non-detections. This process is both time-inefficient and on occasion susceptible to human error, especially at low altitudes where transmission levels in the MUV are significantly affected by absorption due to dust, and thus where the presence of Hartley band absorption can be difficult to confirm by eye.

Recent analyses (Daerden et al., 2022; Määttänen et al., 2022a; Piccialli et al., 2023) presented various procedures to automatically screen false detections by performing two sets of spectral inversions per spectrum: one with ozone in the forward model and one without. As a basic criterion, any spectra in which the difference in the least squares fit between the two sets of spectral inversions ($\Delta\chi^2$) was below a certain threshold were then removed from the ozone retrieval. The exact threshold was defined by setting aside a given number of spectra (a "null set"), observed in narrow latitudinal and seasonal intervals where ozone was assumed a priori not to be present at detectable levels in the data, and then fitting a chi-square distribution to the frequency distribution of derived $\Delta\chi^2$ values for each spectrum in the null set, in order to estimate natural fluctuation of $\Delta\chi^2$ due to random noise. The main drawback with this method is that the null set may only have a small number of spectra depending on the spatial and temporal coverage of the data, which means that it may not necessarily be representative of the occultation data set as a whole, or be sufficiently large to assume Gaussian or chi-square statistics. For this reason, the aforementioned analyses were forced to use additional criteria on top of the basic $\Delta\chi^2$ constraint to filter out false detections: either through measurement of Pearson cross-correlation in the case of Määttänen et al. (2022a), or by imposing a detection limit in the case of Piccialli et al. (2023) using the methodology of Trompet et al. (2021). The null set was required to impose the exact selection threshold for all these methods.

We built on the work of these authors to propose an alternative method of filtering false detections of ozone that did not require the use of a null set, and was therefore suitable for small data sets. Teanby et al. (2019) showed

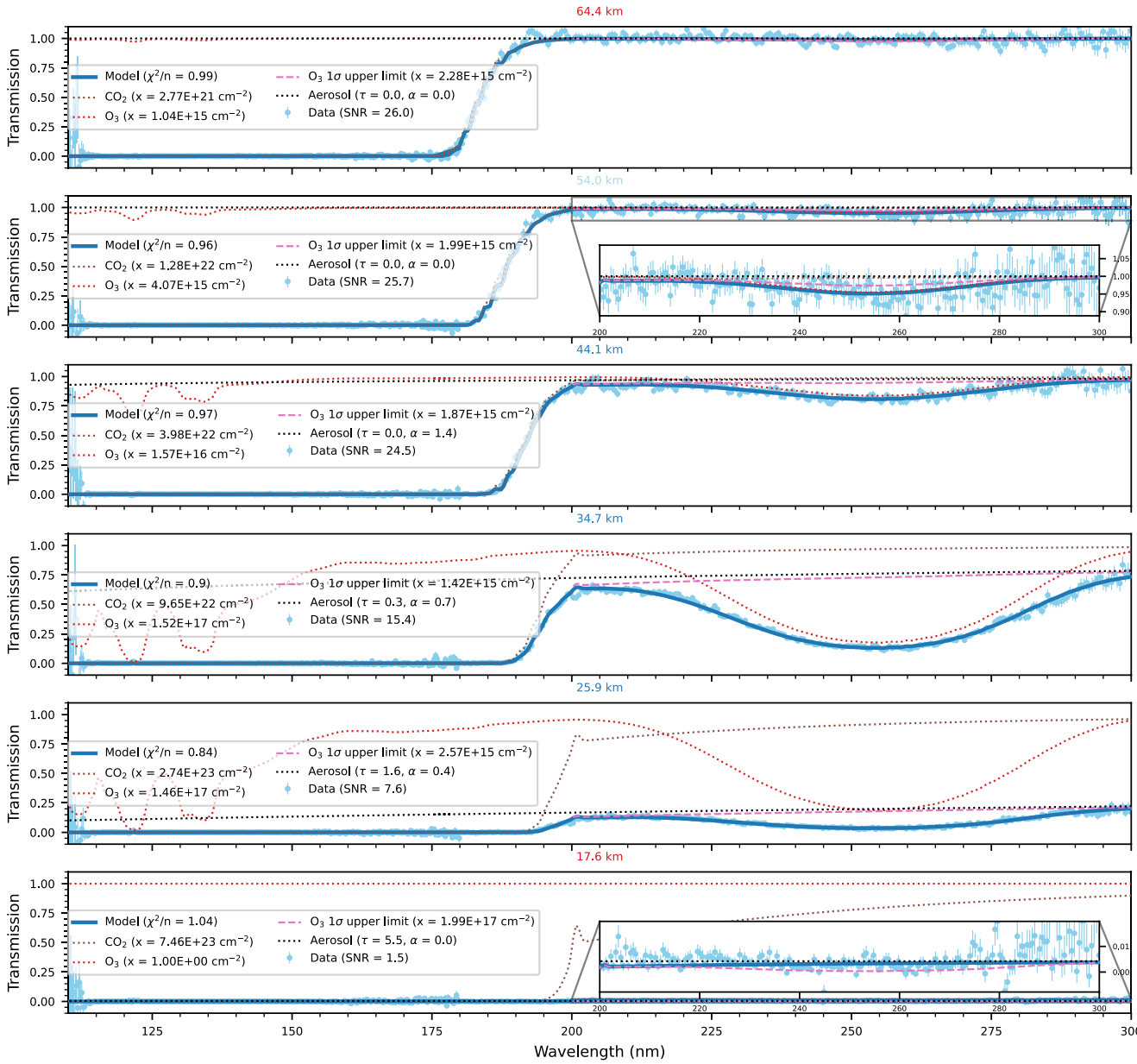



**Figure 1.** Representative spectral fits to an example occultation (20151103T214528) illustrating the main absorption features of an Imaging UltraViolet Spectrograph spectrum within the relevant altitude range. Headings in dark blue represent spectra where ozone was seen to be present above 3 sigma significance, while red headings represent spectra with no confirmed ozone detection above 1 sigma significance according to the detection limit retrieval procedure described in the text. The light blue scatter plots correspond to the observed data, with the estimated noise level given by the error bars, and the model fits are shown in dark blue. Signal-to-noise ratio values in the legend correspond to the average noise level on the observed transmission spectra at wavelengths above 200 nm. The brown, red, and black dotted lines respectively represent the relative contributions of $CO_2$, $O_3$, and aerosol absorption to each modeled spectrum, with retrieved slant densities given in the legend. We do not display the contribution of $O_2$ absorption, as it is negligible relative to that of $CO_2$ which completely dominates far-ultraviolet (UV) absorption at these altitudes. At 64.4 km, the spectrum is almost flat in the mid-UV (MUV), and no ozone is present at statistically significant levels. At 54.0 km, a broad Hartley band centered around 255 nm starts to appear, and the modeled slant density of ozone is just over twice that of the modeled 1$\sigma$ upper limit (as represented by the pink dotted line). This results in a 2$\sigma$ detection of ozone. As one descends in altitude, the Hartley band becomes more prominent and dominates absorption in the MUV. At the same time, the contribution of broad aerosol absorption starts to become significant below 40 km, until it reduces spectral transmission to zero below 20 km. A close-up of the MUV region is provided for clarity at 54.0 km to highlight the 2$\sigma$ detection of ozone, as well as at 17.6 km.

that, for a molecule with a single gas absorption line, a detection limit of $n$-sigma statistical significance could be defined according to the difference between the goodness of fit of the modeled spectrum with slant density $X$ ($y_{mod}(\lambda, X)$) to the observed spectrum ($y_{obs}(\lambda)$) as a function of wavelength $\lambda$, and the equivalent fit of the modeled spectrum with none of the gas present ($y_{mod}(\lambda, 0)$), assuming all other parameters in the model were fixed:



21699100, 2023, 5, Downloaded from https://agupubs.onlinelibrary.wiley.com/doi/10.1029/2022JE007697 by Cochrane France, Wiley Online Library on [23/05/2023]. See the Terms and Conditions (https://onlinelibrary.wiley.com/terms-and-conditions) on Wiley Online Library for rules of use; OA articles are governed by the applicable Creative Commons License

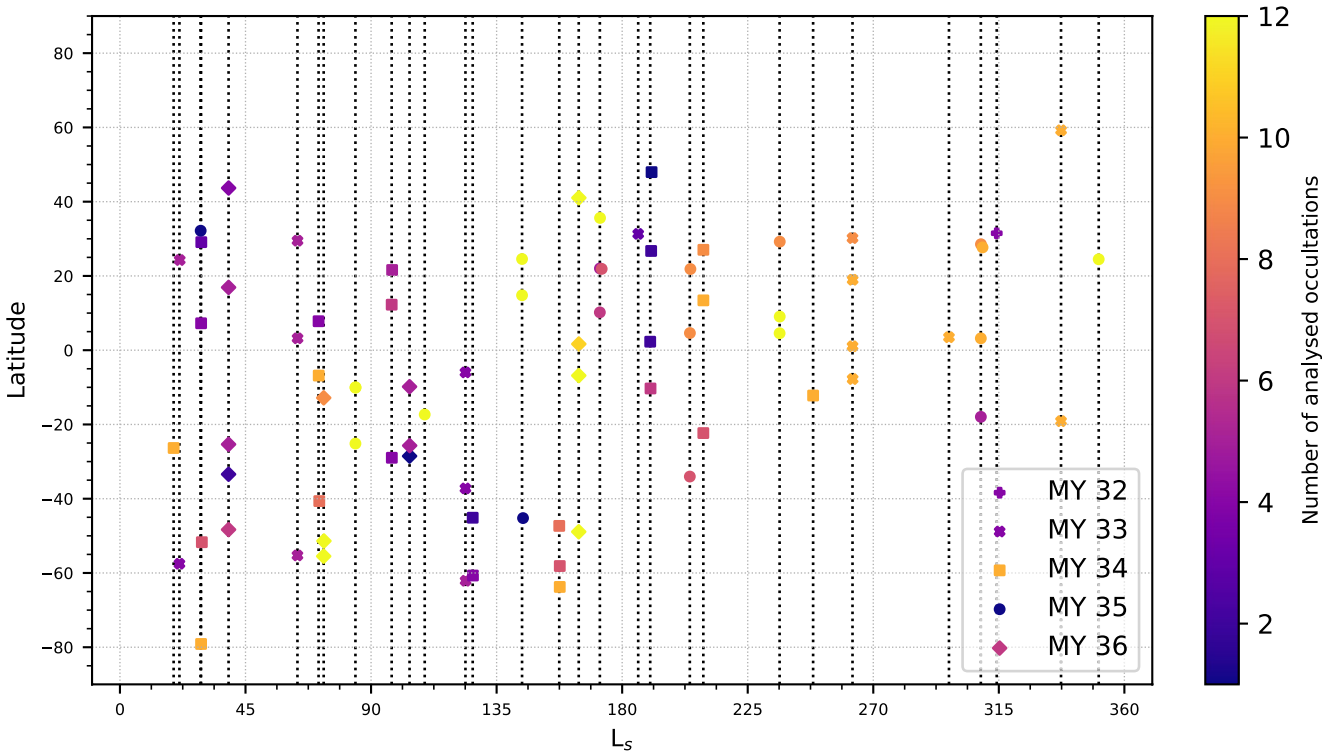



**Figure 2.** Distribution of all 583 Imaging UltraViolet Spectrograph (IUVS) stellar occultations selected following spectral inversion, plotted as a function of latitude and season with the marker symbol indicating Martian year as shown in the legend. The color of each marker indicates the number of occultations performed with the same star (distinguishing sets of observations at ingress and egress where appropriate) at each given latitude and solar longitude. Vertical black dotted lines indicate individual campaigns of observations. A diagram of the full IUVS data set, including observations screened out before spectral inversion, is given in Figure S1 in Supporting Information S1.

$$\Delta\chi^2 = \frac{\Delta\lambda_{\text{sampling}}}{\Delta\lambda_{\text{resolution}}} \sum_i^{N_\lambda} \left( \left( \frac{y_{\text{obs}}(\lambda_i) - y_{\text{mod}}(\lambda_i, X)}{\sigma(\lambda_i)} \right)^2 - \left( \frac{y_{\text{obs}}(\lambda_i) - y_{\text{mod}}(\lambda_i, 0)}{\sigma(\lambda_i)} \right)^2 \right) \tag{7}$$

For non-detections, $n$-sigma upper limits were defined as the values of $x$ that gave values of $\Delta\chi^2 = n^2$ while $n$-sigma detections were analogously defined as the values of $x$ that gave values of $\Delta\chi^2 = -n^2$. $N_\lambda$ was the number of individual spectral pixels in the data and $\sigma(\lambda)$ the spectral uncertainty at each wavelength. The term on the left-hand side of the summation was a correction term for oversampling of the data, where $\Delta\lambda_{\text{sampling}}$ was equal to the spectral pixel sampling and $\Delta\lambda_{\text{resolution}}$ equal to the actual wavelength resolution of the data, equivalent to the half-width-half-maximum (HWHM) of the instrument line shape.

However, the upper limit parametrization of Teanby et al. (2019) assumed a single absorption line that was infinitesimally narrow compared with the instrument line shape. This is not an assumption that applies in the case of the Hartley band. Instead, we assumed that the instrument line shape was narrow compared with the width of the Hartley band and set $\Delta\lambda_{\text{resolution}}$ equal to the HWHM of the Hartley band. We estimated the Hartley band width to be approximately constant at 23 nm for typical temperatures and pressures found in the Martian mesosphere. Hence we defined our $\Delta\chi^2$ ozone detection limit threshold as:

$$\Delta\chi^2 = \frac{\Delta\lambda_{\text{sampling}}}{23} \sum_i^{N_\lambda} \left( \left( \frac{y_{\text{obs}}(\lambda_i) - y_{\text{mod}}(\lambda_i, X_{\text{O3}})}{\sigma(\lambda_i)} \right)^2 - \left( \frac{y_{\text{obs}}(\lambda_i) - y_{\text{mod}}(\lambda_i, 0)}{\sigma(\lambda_i)} \right)^2 \right) \tag{8}$$

For small values of $X_{\text{O3}}$ close to the ozone detection limit, and where the total transmission of the spectrum was not close to zero, $\Delta\chi^2$ followed an approximately quadratic relation with respect to $X_{\text{O3}}$. It was therefore straightforward to iteratively find the values of $X_{\text{O3}}$ that resulted in model spectra at each altitude with $\Delta\chi^2 = 1$. In a spectrum with zero transmission, the detection limit would be infinite as we did not allow for values of $y_{\text{mod}}$ below 0.



21699100, 2023, 5, Downloaded from https://agupubs.onlinelibrary.wiley.com/doi/10.1029/2022JE007697 by Cochrane France, Wiley Online Library on [23/05/2023]. See the Terms and Conditions (https://onlinelibrary.wiley.com/terms-and-conditions) on Wiley Online Library for rules of use; OA articles are governed by the applicable Creative Commons License

21699100, 2023, 5, Downloaded from https://agupubs.onlinelibrary.wiley.com/doi/10.1029/2022JE007697 by Cochrane France, Wiley Online Library on [23/05/2023]. See the Terms and Conditions (https://onlinelibrary.wiley.com/terms-and-conditions) on Wiley Online Library for rules of use; OA articles are governed by the applicable Creative Commons License

At this stage, we considered all ozone slant densities lower than the estimated 2-sigma detection limit to be non-detections of ozone. We found from visual inspection that this 2-sigma threshold was the most optimal in filtering out as many false detections as possible while keeping as many true detections as possible (refer to Appendix A for more detail on this choice). Hence, the use of an intrinsic detection limit based only on aerosol opacity, the SNR and spectral sampling of the data allowed us to filter the data without the possibility of bias from a small null set. We hereon refer to this selection procedure as the Modified Teanby et al. (2019) Detection Limit determination method according to a 2 sigma threshold (MTDL-2).

### 3.3. Vertical Inversion Procedure

Following spectral fitting, we then used the same procedure as detailed in Gröller et al. (2018), itself based on a modified version of the method presented in Quémerais et al. (2006), in order to retrieve vertical profiles of local density of $CO_2$, $O_2$, and retrieved $O_3$, as well as estimated 1-sigma detection limits of $O_3$ (all in units of $cm^{-3}$), through vertical inversion of the aforementioned slant density profiles. Retrieved slant densities of ozone of less than 2-sigma statistical significance were usually excluded in the vertical inversion of ozone. However, for occultations in which only one spectrum was available with a confirmed detection of ozone above 2-sigma significance, we also incorporated a second spectrum into the vertical inversion at an immediately adjacent altitude where the ratio of the retrieved ozone slant density to the 1 sigma upper limit was highest, so that the vertical inversion was able to compute local densities using more than one input. The retrieved vertical profiles were smoothed using Tikhonov regularization, with a constant parameter $\lambda_0 = 0.1$ found by Gröller et al. (2018) to be optimal in smoothing over unphysical oscillations in the vertical profiles while also preserving genuine wave structure at the given altitudinal resolution. The derived $CO_2$ profiles could then also be used to infer a temperature profile. Discussion on the other gaseous and aerosol profiles retrieved from IUVS stellar occultation data besides ozone are beyond the scope of this paper. For more information on $CO_2$, $O_2$, and temperature variations in the upper atmosphere retrieved from IUVS stellar occultations, we refer the reader to another article such as Gröller et al. (2015) or Gupta et al. (2022).

Due to the width and breadth of the Hartley Band signature, percentage a posteriori uncertainty intervals on retrieved ozone densities, as calculated through error propagation in the retrieval algorithm, were usually seen to be very small for ozone densities well above the 2 sigma detection limit threshold (generally around 1%–3% for large values of ozone density typical of the middle atmosphere in the aphelion season). Vertical inversion using the onion-peeling method could, however, occasionally result in the retrieval of undesired negative ozone density values where there was a local peak in retrieved ozone column abundance, an effect also noted by Määttänen et al. (2022a). These values were a consequence either of a lack of vertical resolution at abrupt changes in local densities of ozone, or of a lack of stability in the vertical inversion procedure. Usually these negative values were retrieved either at the edges of the ozone profile, or where a local cloud layer was present in the middle of the profile that obscured spectral signatures of ozone. As they were generally small in magnitude and not usually an encumbrance in the interpretation of general ozone trends, given that they tended to lie at the edges of the ozone profiles away from the relative peaks in ozone density, we were usually able to ignore these values for the purposes of interpretation and simply treat them as missing data.

Our results were then compared with ozone profiles modeled using the Mars Planetary Climate Model (PCM), formerly known as the LMD Mars General Circulation Model, at spatio-temporal coordinates that were as close to the observations as possible within model resolution. We ran the model on the whole data set using the MY 27 climatological dust scenario (Montabone et al., 2015), which was seen to be a year with relatively average dust activity. This was a reasonable assumption given that ozone was not expected to be present at detectable levels during the dust season, and particularly not during global dust storm events such as the one in MY 34 (Montabone et al., 2020). The model was set up according to a latitudinal resolution of 3.75° and a longitudinal resolution of 5.6°, integrated over a vertical grid of 73 levels from the surface up to 200–300 km above the areoid. The time resolution of the model was equal to 15 min, originally tailored to observations near the terminator where ozone abundances were predicted to change rapidly over much shorter timescales than in the nightside hemisphere. Photochemistry was modeled according to Lefèvre et al. (2004) and with further subsequent improvements to the modeling of kinetics, clouds, and heterogenous chemistry taken into account in Lefèvre et al. (2021). Orographic waves were also taken into account in the model. For further details on the physics and the configuration of the PCM for this analysis, the reader is referred to Määttänen et al. (2022a) for which the model configuration was essentially the same.

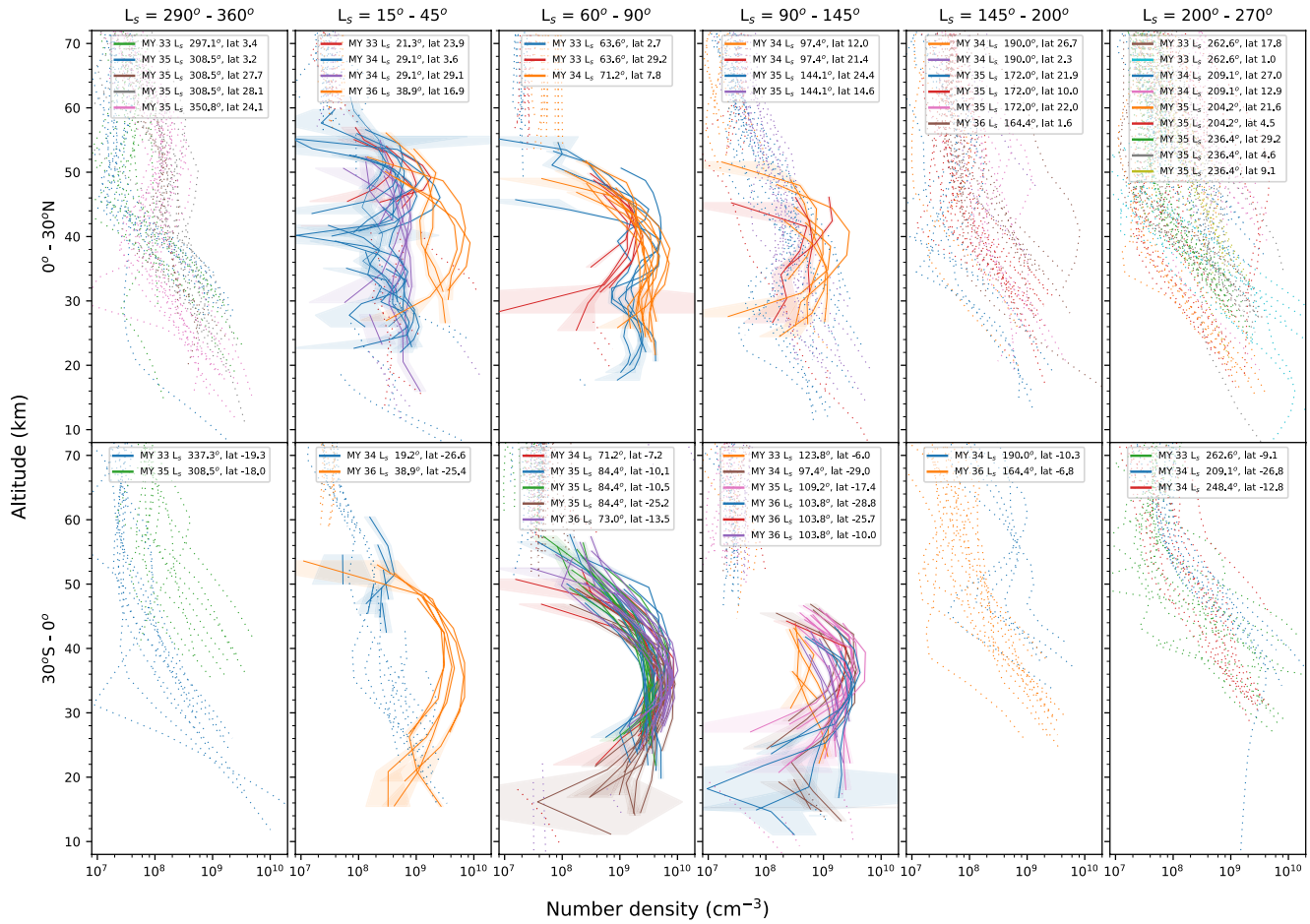



**Figure 3.** Distribution of all retrieved ozone local densities (solid lines) within 30° latitude of the Equator with uncertainties shaded, together with upper limits (dotted lines) at altitudes where ozone was not detected, binned by solar longitude and latitude as explained in the text. Colors are used to denote sets of occultations performed during the same campaign and using the same star. Negative values of ozone density and saturated altitudes where ozone upper limits are infinite are masked on this plot for clarity.

## 4. Results

### 4.1. Seasonal and Latitudinal Trends

#### 4.1.1. Equatorial Latitudes

In order to best sample the solar longitude sampling of the IUVS occultation campaigns, as well as the general seasonal evolution of the retrieved ozone profiles, we divided the data into six irregularly spaced solar longitude bins for visualization purposes: one for the period in which the aphelion detached ozone layer was at its most prominent ($L_s$ = 60°–90°), one approximately spanning the period of peak dust activity ($L_s$ = 200°–270°), and the remaining four spaced in solar longitude around those specific periods in order to best show the change in the probability of ozone detection. Large gaps in solar longitude coverage between $L_s$ = 0°–15°, $L_s$ = 45°–60°, and $L_s$ = 270°–290°, for which no occultations were available in the data set, were excluded. In Figure 3, we present the seasonal trend in all the profiles retrieved at latitudes within 30° of the Equator as a function of latitude and solar longitude. We also compare our results with colocated model predictions by the Mars PCM, for which representative profiles are shown in Figure 4.

Before $L_s$ = 25° we were able to distinguish trends in two sets of occultations: one in the Northern tropics (23.9°N), and one in the Southern tropics (26.6°S). In both sets of data, a small local maximum in ozone density was retrieved at around 50 km altitude, with peak densities averaging $5 \times 10^8$ north of the Equator and $3 \times 10^8$ cm$^{-3}$ south of the Equator. The detection of ozone in the data at these high altitudes was often limited by the presence of aerosols, which varied considerably in opacity with longitude particularly in the Southern tropics. Nonetheless, the Mars



21699100, 2023, 5, Downloaded from https://agupubs.onlinelibrary.wiley.com/doi/10.1029/2022JE007697 by Cochrane France, Wiley Online Library on [23/05/2023]. See the Terms and Conditions (https://onlinelibrary.wiley.com/terms-and-conditions) on Wiley Online Library for rules of use; OA articles are governed by the applicable Creative Commons License

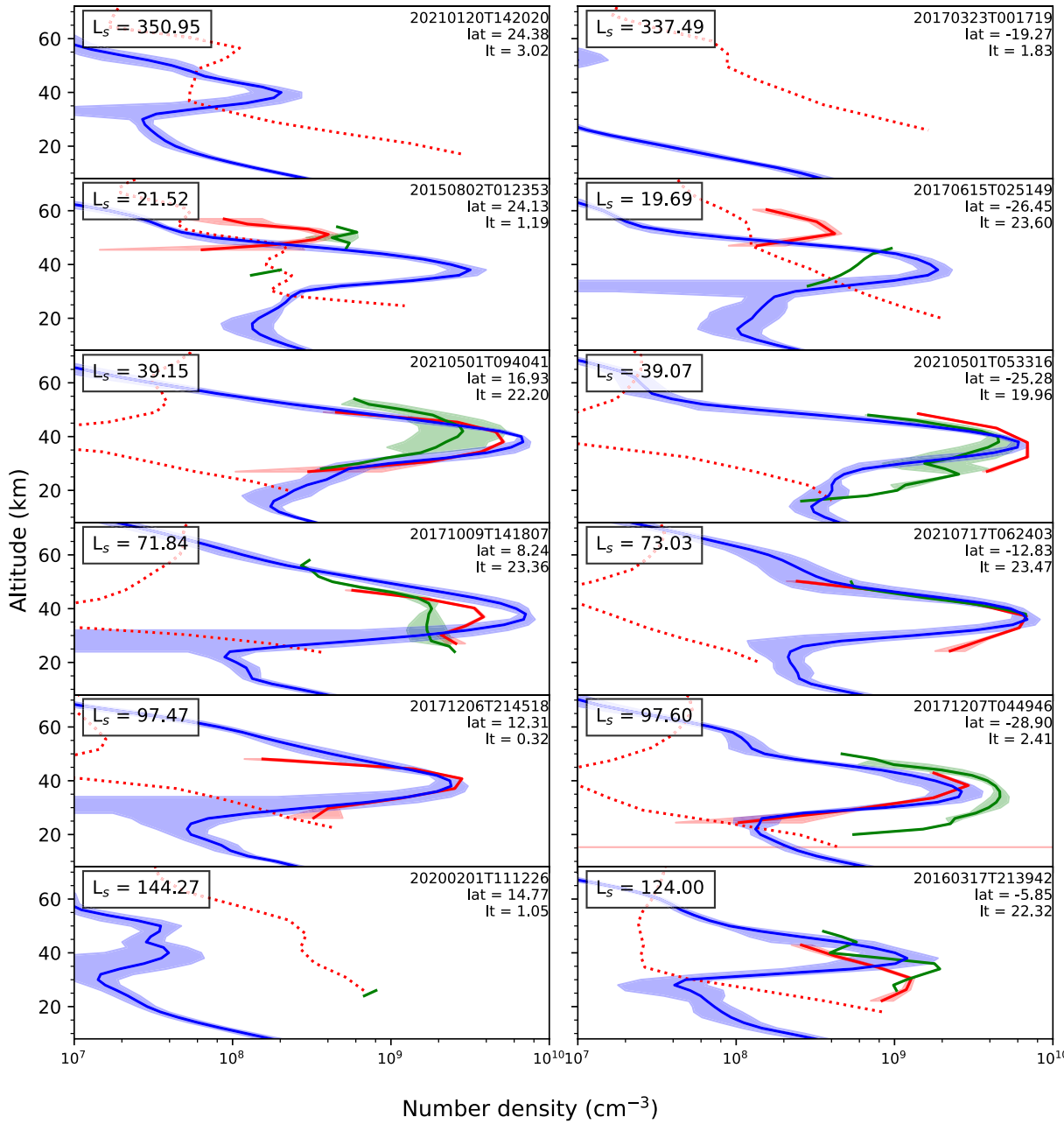



**Figure 4.** Comparison of representative vertical ozone profiles retrieved from Imaging UltraViolet Spectrograph (IUVS) occultation data (red) at different times of the Martian year within 30° of the Equator, with colocated profiles generated from the Mars Planetary Climate Model (blue). Red dashed lines represent retrieved 2$\sigma$ detection limits on ozone. Profiles in the left column were retrieved north of the Equator while profiles in the right column were retrieved south of the Equator. Red shading represents the retrieved uncertainty on the given vertical profile, while blue shading represents the dispersion of ozone local density values at a given altitude for all model profiles colocated with IUVS profiles taken during the same campaign and with the same star. Uncertainties on the model profiles therefore represent the total modeled longitudinal variability along a given latitudinal band. The orbit number of the observed profile is given in the legend, alongside the solar longitude, latitude, and local time. The profiles in green are averaged stellar occultation profiles of ozone derived from SPectroscopie pour l'Investigation des Caractéristiques Atmosphériques de Mars data (Määttänen et al., 2022b), (left) between 0° and 30°N and (right) between 0° and 30°S, within 5° of solar longitude and 2 hr of local time of the IUVS profiles shown.

PCM was seen to consistently overestimate ozone densities during the spring equinox at the predicted altitude of the detached layer at 40 km, and every observing campaign south of the Equator had at least one occultation in which ozone densities were low enough not to be observed at all, as shown in Table 1. This could not be fully explained by the presence of aerosols in the atmosphere, as we occasionally derived 2$\sigma$ upper limits that were an order of magnitude lower than modeled ozone abundances at this altitude. The most notable example was in a single campaign



21699100, 2023, 5, Downloaded from https://agupubs.onlinelibrary.wiley.com/doi/10.1029/2022JE007697 by Cochrane France, Wiley Online Library on [23/05/2023]. See the Terms and Conditions (https://onlinelibrary.wiley.com/terms-and-conditions) on Wiley Online Library for rules of use; OA articles are governed by the applicable Creative Commons License

21699100, 2023, 5, Downloaded from https://agupubs.onlinelibrary.wiley.com/doi/10.1029/2022JE007697 by Cochrane France, Wiley Online Library on [23/05/2023]. See the Terms and Conditions (https://onlinelibrary.wiley.com/terms-and-conditions) on Wiley Online Library for rules of use; OA articles are governed by the applicable Creative Commons License

**Table 1**
*Number and Percentage of Analyzed Occultations per Latitude and Solar Longitude Interval, in Which the Presence of Ozone Was Established Using the MTDL-2 Selection Criterion*

| | $15° < L_s < 45°$ | $60° < L_s < 90°$ | $90° < L_s < 145°$ | $145° < L_s < 200°$ | $200° < L_s < 270°$ | $290° < L_s < 360°$ |
|---|---|---|---|---|---|---|
| $30° <$ lat $< 60°$ | 6/6 (100%) | – | – | 0/21 (0%) | 0/9 (0%) | 1/14 (7%) |
| $0° <$ lat $< 30°$ | 26/26 (100%) | 20/20 (100%) | 10/34 (29%) | 0/41 (0%) | 0/86 (0%) | 0/47 (0%) |
| $-30° <$ lat $< 0°$ | 13/16 (81%) | 56/56 (100%) | 32/32 (100%) | 0/18 (0%) | 1/29 (3%) | 0/19 (0%) |
| $-55° <$ lat $< -30°$ | 8/9 (89%) | 13/13 (100%) | 9/9 (100%) | 5/21 (24%) | 0/9 (0%) | – |
| $-90° <$ lat $< -55°$ | 7/9 (78%) | 17/17 (100%) | 7/7 (100%) | 13/15 (87%) | – | – |

*Note*. Intervals with a complete absence of ozone detections are highlighted in red.

centered over 24°N, conducted just after the end of the regional dust storm season at $L_s = 350°$. In this set of observations, no statistically significant amounts of ozone were detected, even though the Mars PCM predicted an ozone layer to be present at these altitudes with peak densities close to $3 \times 10^8$ cm$^{-3}$, well above retrieved ozone upper limits. Instead, we observed a more tentative ozone layer at 50 km altitude at the very limits of IUVS instrumental sensitivity, which could only be retrieved if we lowered the detection limit threshold to $1\sigma$ (MTDL-1, Figure A4).

Määttänen et al. (2022a) began to retrieve detectable levels of ozone from SPICAM stellar occultations at approximately the same altitudes between around $L_s = 5°$–$15°$, a period for which no IUVS occultations were available. However, two profiles in the Northern tropics were available within a degree of solar longitude and an hour of local time from the respective IUVS occultations at 23.9°N. Both of these profiles showed similar peaks in ozone density at 50 km altitude, averaging around $9 \times 10^8$ cm$^{-3}$. Only one equivalent SPICAM profile was available for the IUVS observations at 26.6°S, and suggested ozone abundances intermediate between those of IUVS and the PCM. IUVS and SPICAM observations therefore both demonstrated that the Mars PCM predicts the onset of the formation of the detached ozone layer too early following the end of the perihelion season, and at too low an altitude.

Due to the sparsity of the solar longitude coverage of IUVS stellar occultations, it is difficult to pinpoint the exact time of year at which the aphelion detached ozone layer started to form from the available data. Occultations performed during a single campaign at $L_s = 29°$ were affected by significant longitudinal variability in the probability of detecting ozone around 40 km, possibly due to the presence of a local thin cloud layer that was regionally confined. Nonetheless, even at longitudes where the effects of the cloud layer were negligible, the density of ozone in the detached layer was clearly small compared with later in the aphelion season, with peak ozone density values only of around $8 \times 10^8$ cm$^{-3}$ at 30–40 km altitude. Only at $L_s = 38.9°$, for which two sets of IUVS occultations were available each side of the Equator, was a strong detached ozone layer consistently observed. During this time, local densities were seen to peak around 35 km in the Southern tropics, with an average peak density of $4.5 \times 10^9$ cm$^{-3}$ and with a longitudinal variability of standard deviation $1.5 \times 10^9$ cm$^{-3}$. Equivalent ozone densities in the Northern tropics were observed to vary more greatly with longitude at 35 km, from values of $1.5 \times 10^9$ to $7.0 \times 10^9$ cm$^{-3}$. Longitudinal variability in ozone structure below 30 km was also seen to be considerable on both sides of the Equator, and was generally larger than predicted by the PCM with retrieved values often greater than $10^9$ cm$^{-3}$. Similarly large values were also observed from SPICAM data below 30 km altitude at this time.

The best correspondences between model and observational results in the Southern tropics were observed within a solar longitude range of between 35° and 90°. During this time, the Mars PCM consistently and correctly predicted ozone densities within this latitude range to peak around 35 km altitude, with peak densities averaging $(5.0 \pm 1.8) \times 10^9$ cm$^{-3}$. This is in line with a longitudinal dispersion of $1.9 \times 10^9$ cm$^{-3}$ around a mean peak value in ozone density of $5.2 \times 10^9$ cm$^{-3}$, as retrieved from IUVS data at the same altitudes. North of the Equator, by contrast, the model correctly predicts ozone to peak at a marginally higher altitude of 38 km, but overestimates peak densities of $(6.8 \pm 1.4) \times 10^9$ cm$^{-3}$ compared with peak IUVS densities of $(3.2 \pm 1.7) \times 10^9$ cm$^{-3}$ averaged over longitude. This observed hemispheric asymmetry of ozone around the Equator was not visible in profiles generated by the model but is well-attested both from previous studies of vertically integrated column abundance (Clancy et al., 2016; Perrier et al., 2006) and from vertical nightside profiles (Määttänen et al., 2022a), although the reverse trend has been attested at similar altitudes during twilight (Khayat et al., 2021; Patel et al., 2021).

Following aphelion, consistent and significant ozone detections were observed north of the Equator only until $L_s = 97°$, with considerable longitudinal variability in the altitude of the detached ozone layer, whereas south

21699100, 2023, 5, Downloaded from https://agupubs.onlinelibrary.wiley.com/doi/10.1029/2022JE007697 by Cochrane France, Wiley Online Library on [23/05/2023]. See the Terms and Conditions (https://onlinelibrary.wiley.com/terms-and-conditions) on Wiley Online Library for rules of use; OA articles are governed by the applicable Creative Commons License

of the Equator consistent ozone detections persisted until $L_s$ = 124°. Gaps in solar longitude coverage made it difficult to determine the exact time of year at which the detached ozone layer north of the Equator disappeared to undetectable levels. However, nightside observations from SPICAM (Määttänen et al., 2022a) also showed a stark asymmetry in ozone detections either side of the Equator at the time of year, with ozone present at detectable levels up to $L_s$ = 90° north of the Equator and $L_s$ = 130° south of the Equator. This correlated with known asymmetries in the Aphelion Cloud Belt (ACB) (Clancy et al., 1996; Willame et al., 2017) during this period, which is habitually centered just north of the Equator and could have also decreased sensitivity to ozone at these altitudes, while also limiting the transport of $HO_x$ to the Southern hemisphere. Sensitivity to ozone above the peak of the detached layer was also seen to decrease during this period in observations south of the Equator, with the maximum altitude of sensitivity decreasing from just below 60 km at $L_s$ = 84.4° down to 45 km at $L_s$ = 97.4°. Contrary to Määttänen et al. (2022a) who observed a factor of 2 underestimation in predicted ozone densities relative to SPICAM during this season, no evidence was present in the IUVS data of a statistically significant deviation in vertical ozone structure from Mars PCM predictions that could not be explained by general longitudinal variability in ozone. No definitive ozone detections were observed in the data beyond $L_s$ = 124°, as the increased dust opacity and moisture of the atmosphere both suppressed ozone production and limited sensitivity to ozone as Mars moved toward perihelion.

#### 4.1.2. Mid- and High Latitudes

A similar analysis of seasonal trends and their correspondences with modeled ozone densities was performed as in Section 4.1.1, but for latitudes greater than 30° away from the Equator. Coverage of the Northern hemisphere was relatively sparse—no IUVS occultations above 60°N were present anywhere in the selected data set, while useable observations between $L_s$ = 0°–180°, where ozone was most likely to be detected, were limited at latitudes above 25°N to only six occultations from two individual campaigns early in the MY. For this reason, a greater emphasis was placed in this analysis on observations from the Southern hemisphere. The resulting ozone profiles are presented in Figure 5, and compared with predictions from the Mars PCM in Figure 6.

We obtained a genuine 3$\sigma$ detection of ozone in a single spectrum at 25 km altitude, just above the height at which the atmosphere became opaque to aerosols, for a single occultation at $L_s$ = 337°. This was the only occultation anywhere in the selected data set in which ozone could be unambiguously confirmed to be present between the Northern autumn and spring equinoxes, and also happened to be the most northerly at 59°N. However, we did not detect ozone in any other observations from the same set of occultations, even though the Mars PCM predicted a layer below 30 km altitude at this time that should have been detectable given retrieved ozone upper limits. At these altitudes, ozone varies little with local time, but it is possible that detections of ozone during this season could be heavily affected by planetary wave activity, which is known to be high and result in major ozone variability (Clancy et al., 2016). We should also emphasize that SPICAM only confirmed ozone in two occultations in the mid-latitudes in either hemisphere between $L_s$ = 320°–360° (Määttänen et al., 2022a), while NOMAD only retrieved ozone in excess of 60° from the equator in quantities for which IUVS lacked sensitivity (Patel et al., 2021).

As with the observations at lower latitudes, solar longitude coverage was sparse around Northern spring equinox, hindering the location of the exact time of year of onset of the aphelion detached ozone layer. We observed the first unambiguous (>2$\sigma$) detections of ozone in the near-surface layer at $L_s$ = 21°, followed by the first observations of ozone above 30 km in a single occultation at $L_s$ = 29°. By $L_s$ = 39°, clear signs of the development of the detached ozone layer were observed at some longitudes in both Northern and Southern mid-latitudes, coinciding with the onset of the same layer closer to the Equator. However, throughout the course of the MY, retrieved ozone profiles were subject to zonal variability potentially spanning more than one order of magnitude along a single latitudinal band at altitudes corresponding to the aphelion detached layer (>30 km).

These longitudinal variations mostly dominated over seasonal changes, as well as any discrepancies between observed and modeled results. Even in the solar longitude range of $L_s$ = 60 –90° when the aphelion detached layer was expected to reach peak density, a detached layer in the middle atmosphere was not resolvable at all longitudes from the near-surface layer below. This was particularly clear at the highest Southern latitudes (for instance at $L_s$ = 63.6° and $L_s$ = 73°, both conducted at similar latitudes of 56°S), where, at some longitudes, a clear detached layer was retrieved at 30–40 km altitude with peak densities of the order of $\sim 3 \times 10^9$ cm$^{-3}$, while at other longitudes, the variation of ozone density with height was seen to be more constant around $\sim 3 \times 10^8$ cm$^{-3}$ between the top of the near-surface layer of ozone at 30 km, up to around 50–60 km. For comparison, while the vertical

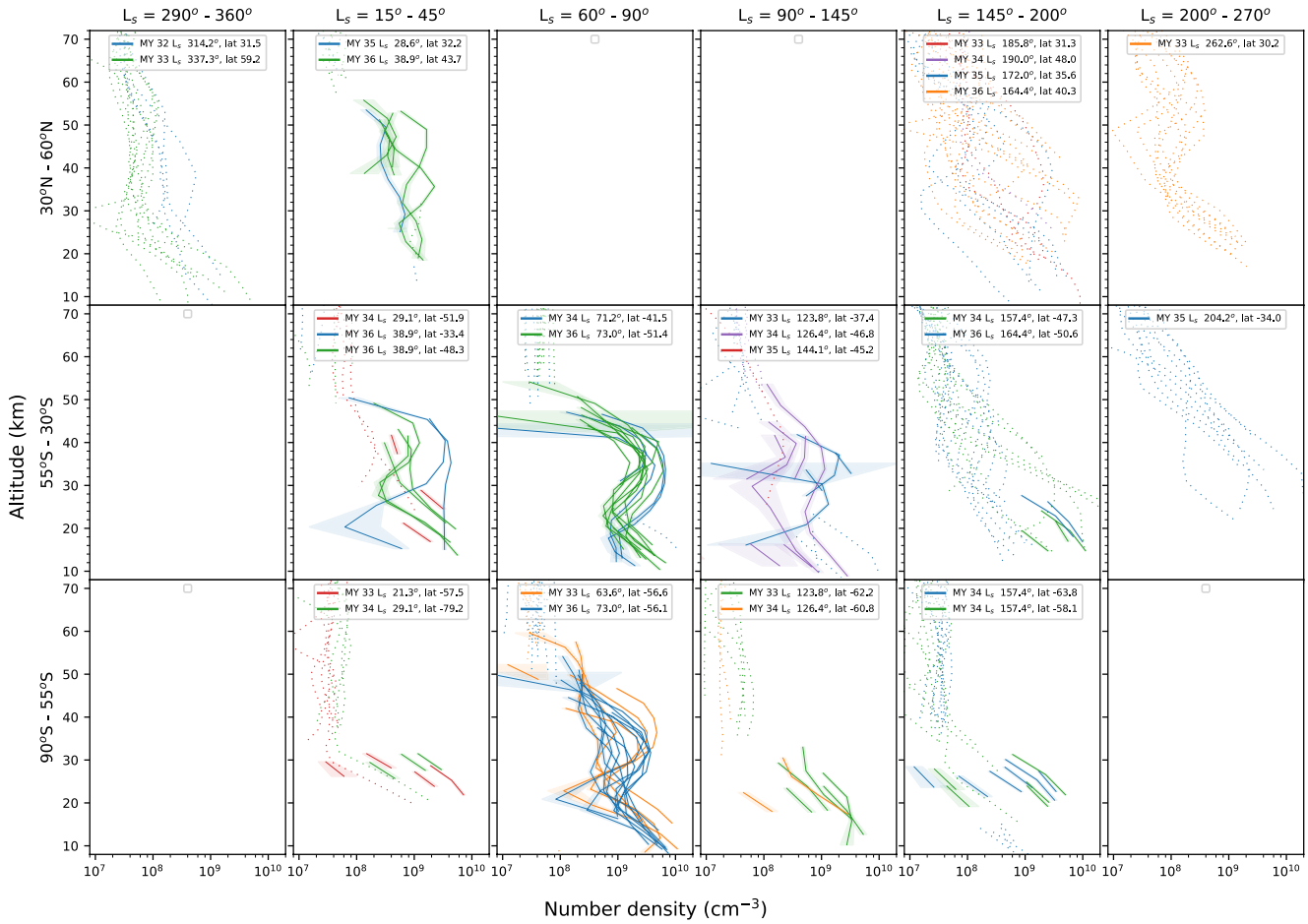



**Figure 5.** As Figure 3, but for latitudes in excess of 30°. Profiles north and south of 55°S, marking the approximate southward limit of the aphelion detached ozone layer, are distinguished in these plots.

structure of averaged profiles from SPICAM stellar occultations (Määttänen et al., 2022a) do correspond well with Mars PCM predictions in the Southern mid-latitudes, individual SPICAM profiles were also seen to vary considerably in vertical structure from observation to observation, especially southwards of 60°S. It is therefore possible that there is considerable interannual variability in the vertical structure at these latitudes. The origin of longitudinal variations between $L_s = 60$ –90° are discussed further in Section 4.2.

The transition in latitude between the presence and absence of a detectable ozone layer above 30 km generally occurred between 55 and 60°S, coinciding approximately with the edge of the polar vortex (Mitchell et al., 2015; Waugh et al., 2016). Close to 60°S, even during the aphelion season, ozone could only be detected above 30 km if allowing for more ambiguous 1–2$\sigma$ detections of ozone, right at the limits of the IUVS sensitivity (Figure A5). Relaxing the detection threshold to 1-sigma (MTDL-1) resulted in the retrieval of a detached ozone layer at 40–50 km, peaking at abundances of approximately $10^8$ cm$^{-3}$. This corresponded to the polar high-altitude layer retrieved by Khayat et al. (2021) and Määttänen et al. (2022a) at 50 km altitude, with typical ozone densities of around 5–10 × $10^7$ cm$^{-3}$, roughly at the limits of IUVS sensitivity at these altitudes. No high-altitude detached layers of ozone above 30 km were detectable either between $L_s = 126°$–314° or anywhere southwards of around 60°S latitude to above 2$\sigma$ statistical significance. The same layer completely ceased to be detectable in the IUVS data set above an altitude of 30 km after $L_s = 130°$, even when allowing for more ambiguous detections of ozone, despite Daerden et al. (2022) showing the layer's persistence right up until the beginning of the dust season. After $L_s = 164°$, we failed to retrieve even a near-surface layer of ozone. This is most likely solely due to loss of sensitivity to the lower layers of the atmosphere by aerosols as opposed to a genuine drop in ozone density, since Olsen et al. (2022) were able to retrieve an ozone layer below 30 km from ACS data that was detectable at high Southern latitudes until approximately $L_s = 200°$.



21699100, 2023, 5, Downloaded from https://agupubs.onlinelibrary.wiley.com/doi/10.1029/2022JE007697 by Cochrane France, Wiley Online Library on [23/05/2023]. See the Terms and Conditions (https://onlinelibrary.wiley.com/terms-and-conditions) on Wiley Online Library for rules of use; OA articles are governed by the applicable Creative Commons License

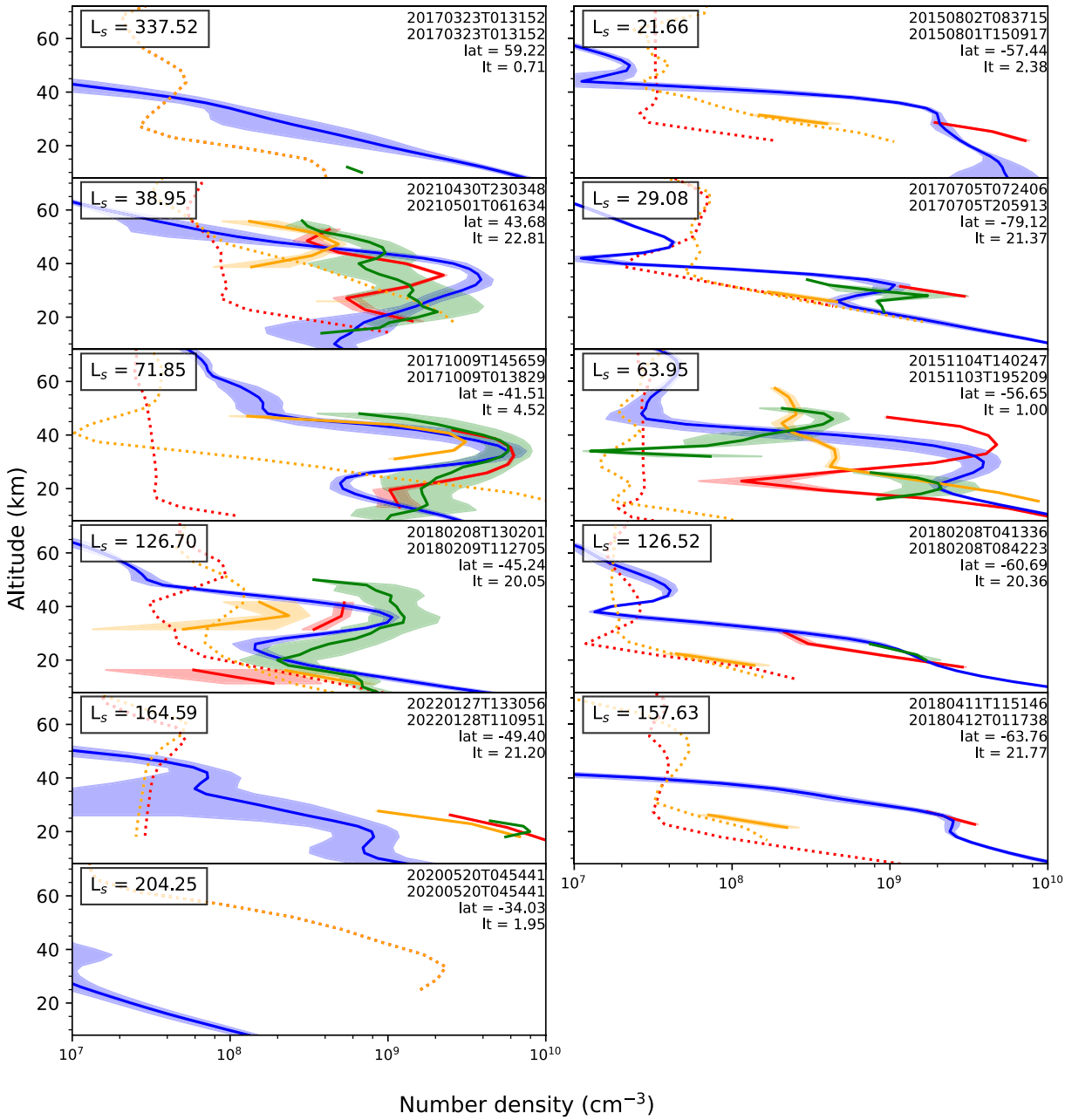



**Figure 6.** As Figure 4, but for latitudes in excess of 30° from the Equator. In each plot, two retrieved profiles (in red and orange, respectively) from the same latitude, solar longitude, and local time are presented, in order to represent the degree of longitudinal variability along a single latitudinal band. In the legend, the orbit number of the red profile is given above that of the orange profile. Green profiles are averaged SPectroscopie pour l'Investigation des Caractéristiques Atmosphériques de Mars profiles from the equivalent latitude bin and within 5° of solar longitude of the Imaging UltraViolet Spectrograph profiles.

We also retrieved similarly high longitudinal variability in the near-surface layer of ozone (<30 km) at high latitudes. This is in contrast to observations of the layer made by the TGO/ACS instrument (Olsen et al., 2022), who only observed a relatively predictable increase in ozone densities in the Southern hemisphere with increasing latitude with less profile-to-profile variability than we obtain from the IUVS data. In some cases, retrievals of the near-surface layer at latitudes in which the high-altitude layer is not observed simultaneously are sometimes underestimated by the vertical inversion procedure (refer to Appendix A), which could appear to exaggerate longitudinal variability in the IUVS data. However, even in profiles where sufficient numbers of spectra are present in the data, there is considerable profile-to-profile variation in the abundances retrieved in the near-surface layer. Discrepancies with the TGO/ACS data could therefore be explained by simple interannual variability, or in differences in sampling.



21699100, 2023, 5, Downloaded from https://agupubs.onlinelibrary.wiley.com/doi/10.1029/2022JE007697 by Cochrane France, Wiley Online Library on [23/05/2023]. See the Terms and Conditions (https://onlinelibrary.wiley.com/terms-and-conditions) on Wiley Online Library for rules of use; OA articles are governed by the applicable Creative Commons License

21699100, 2023, 5, Downloaded from https://agupubs.onlinelibrary.wiley.com/doi/10.1029/2022JE007697 by Cochrane France, Wiley Online Library on [23/05/2023]. See the Terms and Conditions (https://onlinelibrary.wiley.com/terms-and-conditions) on Wiley Online Library for rules of use; OA articles are governed by the applicable Creative Commons License

### 4.2. Longitudinal Variability

Gröller et al. (2018) provided the first proof of concept of using IUVS stellar occultations to look for zonal wave structures in the thermosphere, by performing Fourier component analysis on $CO_2$ density perturbations from a single campaign at the peak of the perihelion season ($L_s$ = 263°). At this time of year, the atmosphere becomes opaque to aerosols in the IUVS wavelength range below 50 km. Although diurnal solar forcing is the dominant factor driving changes in temperature, and hence $CO_2$ density, in the upper atmosphere, the contribution of surface topography to zonal variations in molecular density is still important even at these high altitudes (Medvedev et al., 2016), and would be even more important in the middle atmosphere where IUVS is sensitive to ozone. Nonetheless, variations in ozone in the Martian atmosphere would be further complicated not just by local topography but also by the behavior of water vapor. Specifically, the interplay between the direct formation of $HO_x$ through photolysis, and of the formation of ice cloud layers through condensation that could both restrict the transport of water vapor and mop up $HO_x$ molecules through heterogeneous chemistry (Brown et al., 2022; Lefèvre et al., 2008), was predicted to be an important contributing factor in regional variations of ozone.

Regional differences in ozone due to topography were already established in previous studies by Lefèvre et al. (2015) and Clancy et al. (2016), who found high concentrations of dayside column densities of ozone during Southern winter over the Hellas and Argyre Basins, which are the most low-lying areas of the Southern mid-latitudes of Mars. Additionally, Clancy et al. (2016) predicted that the topography of the Hellas Basin could result in a local northward flow of ozone and carbon monoxide-rich air from the polar vortex toward the Equator. The presence of these two topographical features was also observed to result in wavenumber 2-like perturbations in water column densities at similar latitudes during Southern summer (Montmessin et al., 2004, 2017; Smith, 2004). Transient eddies and baroclinic traveling waves at the edges of the polar vortices (Wilson et al., 2002) were also seen to drive relative variations in ozone abundance around the poles.

Previous measurements of regional variations in vertically integrated ozone column densities, however, would have been dominated by surface layer variations, and not necessarily by variations of mesospheric ozone. We therefore made use of the IUVS stellar occultation measurements to look for regional perturbations in ozone at higher altitudes in the Martian atmosphere. For each occultation per campaign and star, we interpolated the retrieved ozone densities onto a regular altitude grid of 1 km resolution, and then calculated the local perturbation in ozone density $\Delta n/\bar{n}$ relative to the average at a given altitude with respect to longitude. We compared these local perturbations with those estimated from the aforementioned colocated PCM model profiles. In this analysis we only focused on longitudinal variations encompassing the aphelion season for tropical latitudes and Southern summer for Southern extratropical latitudes. Although profile-to-profile variations from IUVS were previously shown by Gröller et al. (2018) to be due to genuine atmospheric variability, and not to differences in the vertical inversion procedure or instrumental effects, we nonetheless decided to focus only on longitudinal variations within the $L_s$ = 60°–90° range, when IUVS longitudinal sampling and coverage was at its highest, in order to only consider consistently identifiable trends in ozone density from multiple sets of observations in different Martian years, that could not be attributed to any random instrumental or methodological artifacts to within any reasonable level of doubt. This period also covered the peak of ozone formation in the middle atmosphere, when uncertainties on retrieved ozone densities would be negligible relative to genuine geographical variation in ozone, and when the effect of aerosols on the detectability of ozone would be minimized.

#### 4.2.1. Equatorial Latitudes

In Figure 7 we plotted the amplitudes of ozone perturbation derived from eight different sets of occultations obtained within 30° of the Equator with the best longitudinal coverage and sampling of retrieved ozone. The most striking feature was a local enhancement of ozone (hereon referred to as the Eastern Equatorial Enhancement [EEE], for brevity), centered over approximately 50°–130° longitude east of the central meridian, that appeared to be present at the same time of year in all Martian years covered by the IUVS data set. Its base was usually located above around 30 km altitude, and was clearly visible as far north as 30°N and as far south as 10.5°S, approximately spanning the latitude range of the ACB. This is illustrated more clearly when averaging just the ozone local densities between 35 and 45 km altitude (Figure 8), where a clear and consistent peak in ozone density between 100° and 120°E could be seen relative to longitudes immediately westwards of the central meridian. While this feature was evident within 10° latitude of the Equator, it rapidly becomes less apparent toward higher latitudes. At 25°S (passing just north of the Hellas Basin), no discernible ozone enhancement was observed in the Western half of where the EEE would be expected, and it is unclear if the enhancement at 120°E was part of the same feature. At 29°N, longitudinal sampling was too low to discern any real trends in the data.

10.1029/2022JE007697

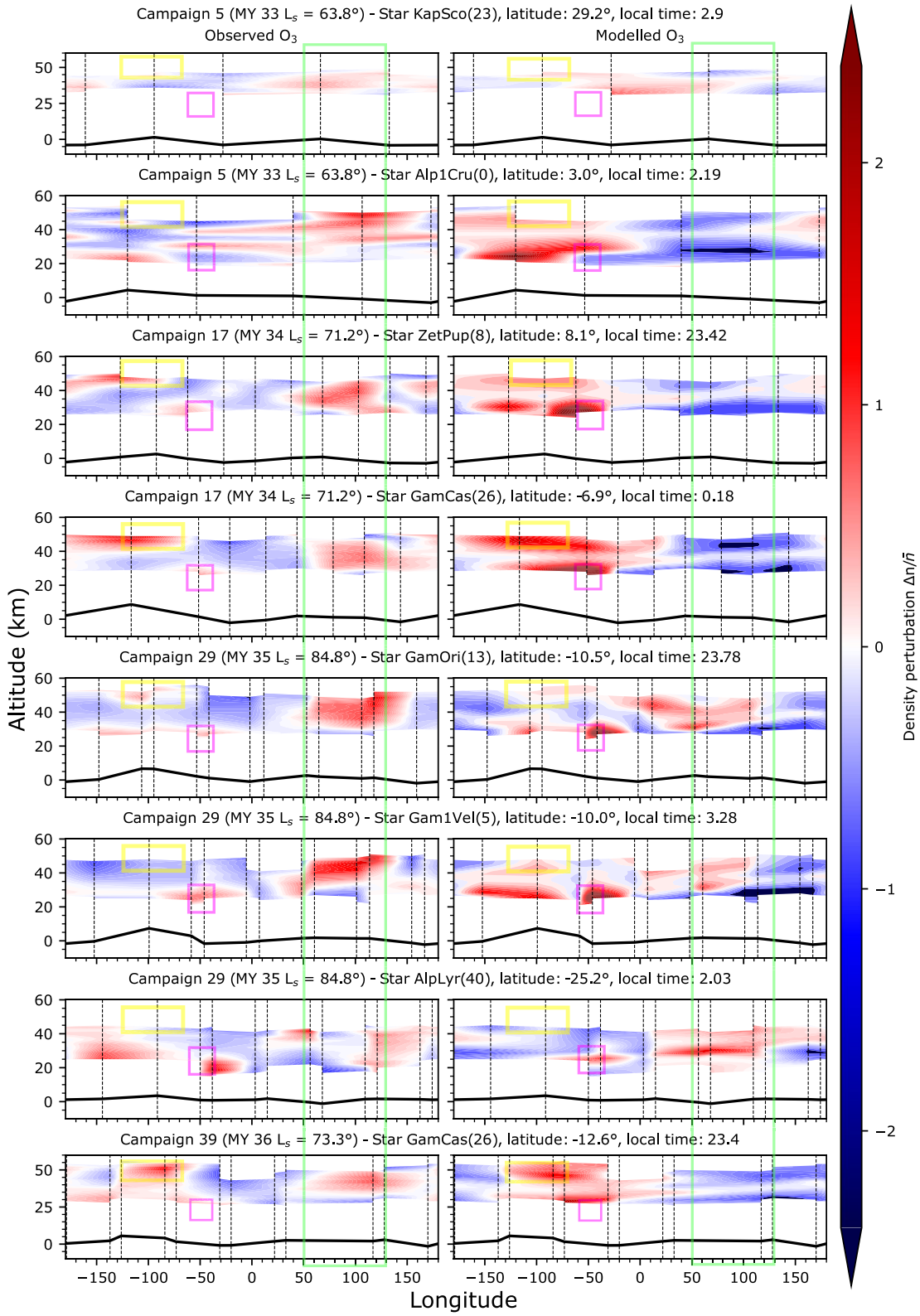



**Figure 7.**



21699100, 2023, 5, Downloaded from https://agupubs.onlinelibrary.wiley.com/doi/10.1029/2022JE007697 by Cochrane France, Wiley Online Library on [23/05/2023]. See the Terms and Conditions (https://onlinelibrary.wiley.com/terms-and-conditions) on Wiley Online Library for rules of use; OA articles are governed by the applicable Creative Commons License

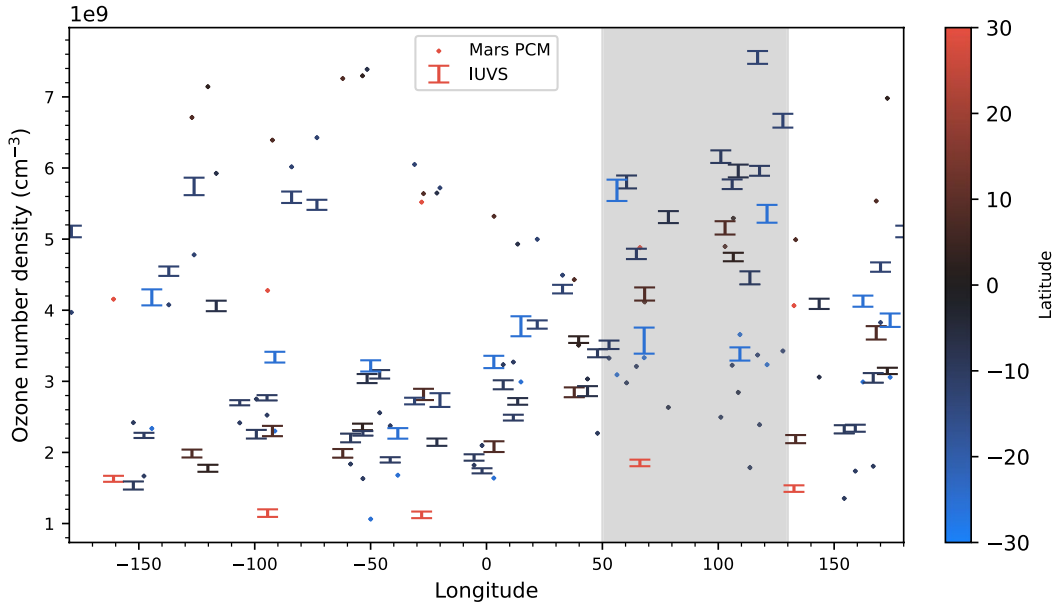



**Figure 8.** Retrieved ozone local densities, with uncertainties, averaged between 35 and 45 km altitude, within a solar longitude range of $L_s$ = 60°–90° and within 30° latitude of the equator. Predicted average densities from the Mars Planetary Climate Model for the same times and locations are shown as dots for comparison. The approximate longitudinal span of the region of consistent ozone enhancement between 50° and 130°, as explained in the text, is shaded in gray.

The Mars PCM, by contrast, predicted the opposite trend: a relative depletion in ozone in the Eastern Hemisphere compared with the Western hemisphere, and of similar magnitude to the relative peak in ozone density that was observed in the Eastern hemisphere from the IUVS data. The origin of this feature is therefore difficult to explain scientifically. Diurnal measurements of the ACB performed by the Emirates eXploration Imager (EXI, Jones et al. (2021) and Wolff et al. (2022)) and Emirates Mars InfraRed Spectrometer (EMIRS, Atwood et al. (2022) and Smith et al. (2022)) instruments, on board the Emirates Mars Mission, showed that the ACB tended to have the greatest concentration of cloud in the morning between a region approximately spanned by 60°–120°W longitude, coinciding with the Tharsis range, with a smaller concentration of cloud centered over Elysium Planitia at 150°E that would become prominent during the evening. The net result of this zonal heterogeneity in the ACB should have been a higher concentration of ozone over the Tharsis region, mostly due to the effect of clouds restricting the ascent of water vapor high into the atmosphere since the ACB was predicted to only have a modest effect on ozone abundances through heterogeneous chemistry (Clancy et al., 2016; Lefèvre et al., 2021). This was also reflected in PCM predictions, which show a relative enhancement of ozone in the Western hemisphere. On the other hand, tentative nightside observations from the Mars Climate Sounder instrument, did indicate a slight peak in column-integrated water ice abundances centered at 20°N and 100°E (Guha et al., 2021). This may result in small differences in how much water is transported southwards from the North Pole at that longitude, resulting in a slight depletion in water vapor southward of the peak in water ice opacity. We should also note that southward transport of water vapor is heavily affected by differences in topography as well as the thermal inertia of the surface (Putzig & Mellon, 2007), which results in meridional flux of water vapor that, at these latitudes, is concentrated around the Western flank of the Tharsis range (Montmessin et al., 2017). We do not discount the effect that zonal transport of water may have on differences in concentration of ozone.

**Figure 7.** Illustration of longitudinal variability of ozone as a function of altitude for eight individual sets of occultations obtained within 30° latitude of the Equator and within a solar longitude range of 60°–90°, comparing (left) retrieved ozone profiles from Imaging UltraViolet Spectrograph (IUVS) stellar occultations with (right) predicted values from the Mars Planetary Climate Model for altitudes at which IUVS is sensitive to the presence of ozone. Colors indicate the ozone local density perturbation $\Delta n/\bar{n}$ with respect to the zonal mean calculated at each altitude: red indicates relative enhancement of ozone while blue indicates relative depletion. Vertical black dashed lines indicate the longitudes of the individual occultations from which ozone profiles were retrieved. Density perturbation values at intermediate longitudes and altitudes are calculated through bilinear interpolation from these points. Three specific recurring regions of ozone enhancement are highlighted as described in the text: (green) the Eastern Equatorial Enhancement between 50° and 130°, (magenta) a region below 30 km altitude bounded between approximately 40°–60°W, (yellow) a high-altitude area of enhancement located directly above the Tharsis range.



21699100, 2023, 5, Downloaded from https://agupubs.onlinelibrary.wiley.com/doi/10.1029/2022JE007697 by Cochrane France, Wiley Online Library on [23/05/2023]. See the Terms and Conditions (https://onlinelibrary.wiley.com/terms-and-conditions) on Wiley Online Library for rules of use; OA articles are governed by the applicable Creative Commons License

21699100, 2023, 5, Downloaded from https://agupubs.onlinelibrary.wiley.com/doi/10.1029/2022JE007697 by Cochrane France, Wiley Online Library on [23/05/2023]. See the Terms and Conditions (https://onlinelibrary.wiley.com/terms-and-conditions) on Wiley Online Library for rules of use; OA articles are governed by the applicable Creative Commons License

Some diurnal change in ozone variation, independent of latitude, could be discerned from two sets of observations conducted during a single campaign in MY 35 (Campaign 29, $L_s = 84.5°$). These two sets of observations, consisting of 12 occultations each, were conducted over the same latitudinal band (10.5°S), but performed using a different star and shifted in local time by 3.5 hr. A relative increase in the altitude of the Eastern part of the EEE was observed between the two sets of data, with the peak of the detached ozone layer ascending from 35 to 40 km altitude, as well as a relative decrease in altitude of the Western part of the EEE. However, we did not observe clear evidence of the feature being the result of a thermal tide, since a sun-synchronous tide would result in a westward migration of the feature between the two sets of occultations by approximately 50°. This would be easily detectable given the longitudinal sampling of observations, but was absent in the data. A change in the vertical ozone profile was also observed over the Tharsis region (centered at 100°W), with the local ozone enhancement above 40 km altitude fading over the course of the night. This appeared to be the result of a diurnal change that was not unique to this set of observations, as the same ozone enhancement above 40 km was clearly observed in the other sets of occultations that were obtained around local midnight presented in Figure 7, but faded in prominence at later local times.

We confirmed an additional ozone feature consistently observed around 40°–60°W at altitudes below 30 km. While this was toward the lower altitude limit of what could reliably be observed using IUVS stellar occultations at this time of year, it was nonetheless consistent with model predictions, and was likely due to a combination of the presence of Valles Marineris and the Argyre Basin just to the south, where wave activity was predicted to elevate local column abundances of ozone (Clancy et al., 2016). By contrast, an analogous feature was not seen at similar altitudes in Campaign 29, centered at the Northern edge of the Hellas Basin (45°–100°E), despite also being attested from column-integrated observations by Clancy et al. (2016) and others. It is possible that local enhancements in ozone densities over the Hellas Basin were simply located too deep in the atmosphere to be detected by IUVS stellar occultations.

#### 4.2.2. Mid Southern Latitudes

Similar analysis of longitudinal variation at higher latitudes was made difficult by the fewer sets of occultations available with comprehensive longitudinal coverage. No sets of occultations were available between $L_s = 60°–90°$ at latitudes northward of 30°N. For this reason, the effect on ozone of hemispherical asymmetries in the contribution of the two polar ice caps in the water cycle could not be measured. We therefore performed the same analysis of longitudinal density perturbations on only four individual sets of occultations, obtained between $L_s = 60°–90°$ and confined to a latitude range between 41° and 56°S. These observations probe a large altitude range and are therefore less likely to be affected by edge effects in the vertical inversion procedure as described in Appendix A. The results are presented in Figure 9.

Due to a combination of straylight issues and a lack of orbital coverage, data was often missing for the Eastern hemisphere of Mars. However, wave structure was clearly apparent particularly in data from observation campaign 39, conducted in MY 35 at $L_s = 73.3°$ and centered over a latitude of 56°S. At this time, perturbations in ozone density indicated a wave structure consisting of a strong planetary 1 component together with a weaker higher-frequency component, affected by an eastward shear with increasing altitude. The same feature was likely to be present in all three occultations at latitudes poleward of 50°S, but data was limited due to a lack of longitudinal coverage in the case of the EtaUMa observation from Campaign 39 at 51°S, and a lack of longitudinal sampling in the case of the LamSco observation from Campaign 5 (MY 33, $L_s = 63.8°$) at 56°S. Fukuhara and Imamura (2005) found similar wave activity in Southern summer, albeit with a phase shift in wave propagation in the opposite direction to what was observed in the IUVS data, due to the seasonal change in direction of prevailing winds (McCleese et al., 2010). While variations at the edge of the Southern polar vortex were expected to be dominated by waves of first wavenumber harmonic (e.g., Banfield et al., 2003; Guzewich et al., 2012; Hinson et al., 2003), Fukuhara and Imamura (2005) were able to derive higher-order components in Southern summer near the poles. It is unclear if the secondary components observed in the IUVS data were the same as those observed by Fukuhara and Imamura (2005), or if they were simply an effect of temporal sampling: while Clancy et al. (2016) quoted approximate eastward rotation periods of these observed waves of the order of 2–4 days, in line with previous observed and modeled results (Barnes et al., 1993; Hinson, 2006), IUVS occultation campaigns were carried out over a 2 day period in a westward trajectory. As the period of observation coincided with a so-called "solsticial pause" in which transient eddy activity was expected to be weak (Battalio et al., 2018; Lewis et al., 2016; Mulholland et al., 2016), the observed wave structure was likely to be a stationary wave resulting from forcing by either topography or thermal tides. These waves could drive vertical variations in

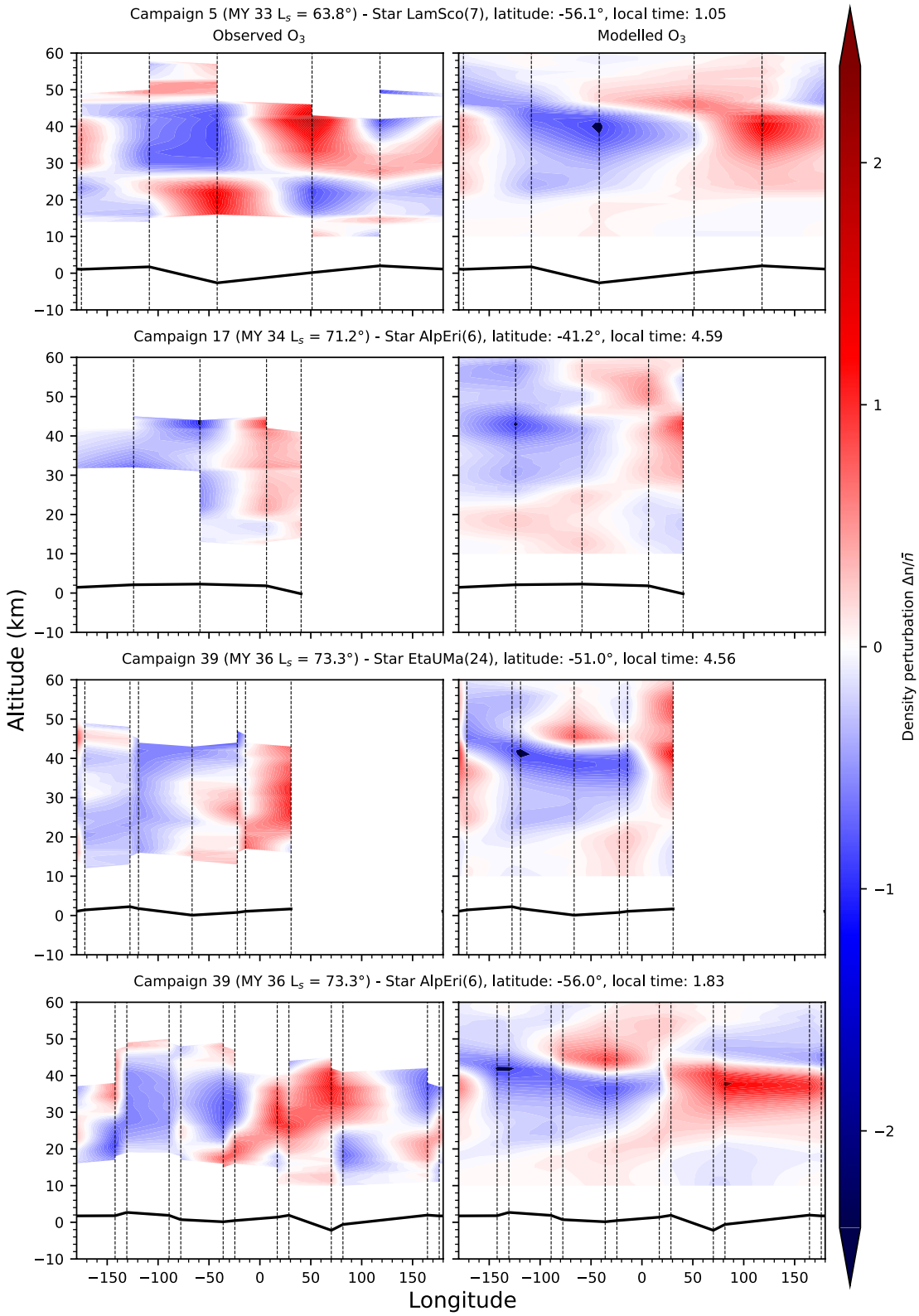



**Figure 9.** As Figure 7, but for four individual sets of occultations at Southern latitudes in excess of 30° from the Equator. For the purposes of clarity, no bilinear interpolation was performed between occultations spaced more than 100° of longitude apart.



21699100, 2023, 5, Downloaded from https://agupubs.onlinelibrary.wiley.com/doi/10.1029/2022JE007697 by Cochrane France, Wiley Online Library on [23/05/2023]. See the Terms and Conditions (https://onlinelibrary.wiley.com/terms-and-conditions) on Wiley Online Library for rules of use; OA articles are governed by the applicable Creative Commons License

21699100, 2023, 5, Downloaded from https://agupubs.onlinelibrary.wiley.com/doi/10.1029/2022JE007697 by Cochrane France, Wiley Online Library on [23/05/2023]. See the Terms and Conditions (https://onlinelibrary.wiley.com/terms-and-conditions) on Wiley Online Library for rules of use; OA articles are governed by the applicable Creative Commons License

temperature, which observations from TGO/ACS (Olsen et al., 2022) showed was a major driver of differences in vertical ozone structure below 30 km.

Hints of a slight enhancement of ozone at 30° and 70°E were discernible from the data at altitudes below 20 km in the Campaign 39 set of observations at 56°S, in which the 70°E occultation probed the Martian atmosphere directly above the Southern shore of the Hellas Basin. However, as the same feature was not seen just to the east at 82°E, it is unclear if this was a clear signature of elevated ozone densities in the Hellas Basin. It is possible that the high ozone densities observed over the Hellas Basin in column-integrated retrievals were confined to altitudes below 10 km, for which IUVS stellar occultations are opaque to aerosols.

In general, the magnitude of longitudinal variability appeared to increase with latitude, particularly south of 50°S. Substantial order-of-magnitude variations in ozone density were observed at both the detached layers above 30 km and the near-surface layers below 30 km. This is in contrast to nearer the Equator where large orders of magnitude differences in ozone density with longitude were only present above the altitude of the peak of the detached ozone layer, that is to say above 40 km. This reinforces the idea that, at these latitudes, many of the main features that are characteristic of known seasonal and latitudinal variations in ozone are in fact dominated by local and possible short-term weather phenomena, as opposed to genuine climatological trends.

## 5. Conclusions

We analyzed 583 useable stellar occultations from the MAVEN/IUVS instrument between Martian years 32–36, expanding on the preliminary work of Gröller et al. (2018) to conduct the first systematic study of zonal variations in the vertical structure of ozone in the night-time hemisphere of the Martian atmosphere, and how they related to general changes in ozone density with respect to season and latitude. Using a filtering algorithm based on that of Teanby et al. (2019), we were able to detect ozone in 224 individual occultations, almost entirely spanning a period from $L_s = 20°–170°$. Within the tropics, the retrieved vertical density profiles of ozone were seen to be dominated by seasonal cycles in the detached ozone layer above 30 km altitude. The seasonal appearance and disappearance of this layer was well-attested from previous observations and model predictions in the literature (e.g., Clancy & Nair, 1996; Daerden et al., 2022; Khayat et al., 2021; Lebonnois et al., 2006; Lefèvre et al., 2004; Määttänen et al., 2022a; Patel et al., 2021), with only small differences in the solar longitude range over which the layer is observed. Following Southern winter and toward the spring equinox, variations in ozone local density started to become limited by variations in the presence of aerosol, and we did not confirm any statistically significant ozone detections in the data between $L_s = 170°–340°$. A less well-attested phenomenon that was derived from the IUVS data was a gradual descent in the altitude of the detached ozone layer from 50 km at $L_s = 20°$ to 30 km at $L_s = 124°$ over multiple Martian years, before sensitivity to ozone was lost as Mars approached equinox. This was an effect that could not be explained solely by short-term fluctuations with longitude.

We confirmed that our observations of the vertical structure of ozone at these latitudes were in quantitative agreement with nighttime stellar occultation measurements from the SPICAM instrument reported by Määttänen et al. (2022a), with small inconsistencies between the two data sets easily explained by longitudinal, interannual or other spurious sources of variability. When compared with colocated predictions from the Mars PCM, the two data sets therefore exhibit similar correspondences and discrepancies. The Mars PCM best reflects the observed vertical structure of ozone above 30 km altitude in the Southern tropics (0°–30°S) during the height of the aphelion season (approximately $L_s = 35°–90°$), correctly modeling peak ozone densities between 35 and 40 km altitude of $(5 \pm 2) \times 10^9$ cm$^{-3}$. However, the Mars PCM was unable to account for a hemispheric asymmetry around the Equator, with peak ozone densities in the Northern tropics (0°–30°N) observed by both IUVS and SPICAM to be lower by approximately a factor of 2 than in the Southern tropics. This asymmetry could not be entirely explained by longitudinal variability. In addition, the Mars PCM predicted a vertical ozone structure that was too constant over the first half of the Martian year. In particular, it was unable to correctly predict the magnitude and altitude of the high-altitude ozone layer close to equinox ($L_s < 25°$), which was observed by both IUVS and SPICAM to be centered at around 50 km altitude in the Northern tropics, and with densities of approximately an order of magnitude lower than model predictions.

At equatorial latitudes, observed peak densities of the detached ozone layer were seen to vary only within approximately a factor of 2 as a function of longitude within $L_s = 60°–90°$. Nonetheless, significant regional features of ozone enhancement at low latitudes were observed during the aphelion season. Most notably, a region of

21699100, 2023, 5, Downloaded from https://agupubs.onlinelibrary.wiley.com/doi/10.1029/2022JE007697 by Cochrane France, Wiley Online Library on [23/05/2023]. See the Terms and Conditions (https://onlinelibrary.wiley.com/terms-and-conditions) on Wiley Online Library for rules of use; OA articles are governed by the applicable Creative Commons License

consistent enhancement of ozone in the Eastern hemisphere of Mars was observed during aphelion season, centered around 50°–130°E longitude and approximately spanning the latitude range of the ACB. We referred to this feature as the EEE. These features likely resulted from the interaction of condensation flows transporting water vapor from the Northern polar caps with the local topography. While the Mars PCM was able to correctly predict areas of local, diurnally varying ozone enhancements at high altitude over and east of the Tharsis region during this season, it failed to predict the presence of any kind of increase in ozone density where the EEE was observed by IUVS, instead predicting a general depletion of high-altitude ozone in the Eastern hemisphere relative to the Western hemisphere.

For higher latitudes, longitudinal variability (most likely related to either persistent regional anomalies or short-term weather systems) was seen to be as, and in some cases, more important than seasonal variability in explaining the main features that could be resolved in vertical profiles of ozone density during the first half of the Martian year. The prominence of a detached ozone layer at Southern mid-latitudes in particular was seen to be heavily longitude-dependent, with retrieved ozone profiles often varying by an order of magnitude over a single latitudinal band. Much of this variation could have been driven by planetary waves at the edge of the polar vortex. Evidence of a planetary 1 wave, with similarities to stationary waves at equivalent latitudes found by Fukuhara and Imamura (2005) during Southern summer, was detected from the IUVS data at Southern mid-latitudes, exhibiting an eastward phase shift with ascending altitude. The presence of these waves would have a significant impact on previous observations of the aphelion ozone layer in the night-side (e.g., Määttänen et al., 2022a), and to a lesser extent at the terminator (e.g., Khayat et al., 2021), particularly in the 50°–60° region. They are also incompletely accounted for in the Mars PCM. By contrast, no unambiguous evidence was found for any local enhancements in ozone close to the Hellas Basin. This implies that the anomalously high column abundances of ozone retrieved at nadir (Clancy et al., 2016) could be either due entirely to near-surface ozone that is too deep to be detected by IUVS, or is simply a consequence of the low elevation of the Hellas Basin and hence greater airmass that would naturally lead to high column abundances.

Since the aerobraking campaign conducted by MAVEN in February 2019, the number of stellar occultations per observational campaign has increased sharply. This has allowed for a more careful and systematic study of latitudinal and longitudinal variations in ozone. Continued stellar occultation campaigns conducted by MAVEN/IUVS over the next coming years, combined with improvements to the calibration pipeline, should result in an increased number of useable nightside observations that will allow us to look for consistent trends in longitudinal and regional trends in ozone concentration over multiple Martian years. This should allow for further analysis of regional variations in ozone before $L_s = 60°$ and after $L_s = 90°$, for which coverage to date has been insufficient to distinguish real regional variations in ozone from simple profile-to-profile variations. Further observations of ozone at Northern high latitudes in particular, for which current MAVEN/IUVS observations are sparse and which were disproportionately affected by straylight contamination, should also shed further light on hemispherical asymmetries in planetary waves, and hence the dynamics of the two polar vortices that would affect the meridional transport of water.

## Appendix A: Validation of Ozone Selection Criteria

A statistically significant detection of a gas from a spectrum is typically taken as one that is significant to either 3-sigma ($\sigma$) and above (1 in 741 chance of occurring spontaneously from Gaussian noise) or 5$\sigma$ and above (1 in $3.5 \times 10^6$ chance of occurring from Gaussian noise) by convention. This choice typically depends on the authors' personal discretion given the size and quality of the data involved, as well as if the molecule is already known to exist in the atmosphere or not. In practice, however, these conventional detection thresholds can be imperfect in filtering genuine detections from non-detections as (a) spectral noise can be difficult to estimate precisely and (b) sigma detection limits do not usually take systematic sources of spectral uncertainty into account. Additional visual inspection of the spectra is therefore required to empirically determine the choice of threshold that best discriminates between true and false detections.

For convenience, we will hereon refer to the method of detection limit imposition previously described in Section 3.2 as the Modified Teanby et al. (2019) Detection Limit determination method (MTDL-2), with the subsequent number specifying the sigma detection threshold value, in this case equal to 2. In Figure A1 we present the spectra in each occultation that were included in the vertical inversion using, respectively, a 1-, 2-, and 3$\sigma$ detection limit threshold (MTDL-1, MTDL-2, and MTDL-3). MTDL-1 was deemed too lenient as it allowed

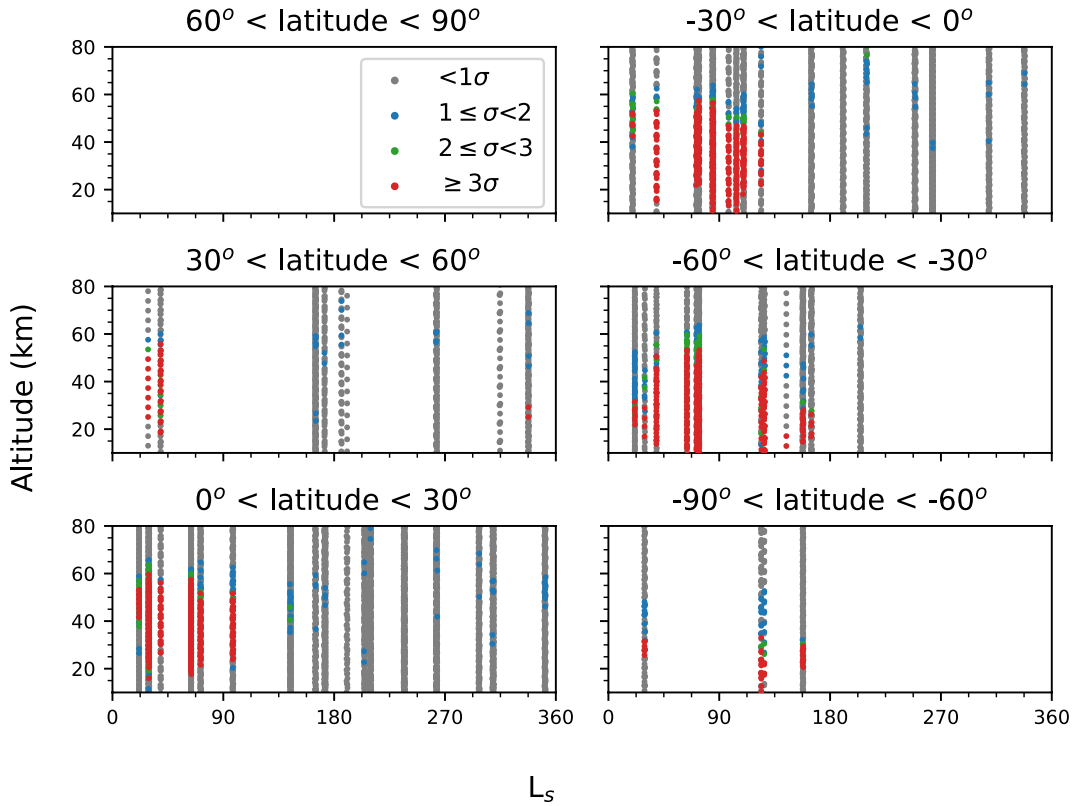



**Figure A1.** Latitude and solar longitude distribution of ozone local density profiles retrieved from the Imaging UltraViolet Spectrograph, with color coding indicating altitudes that were included in the vertical inversion following filtering by 1-, 2-, and 3$\sigma$ thresholds, respectively.

for the acceptance of multiple false detections during the perihelion season. Figure A2 shows an example of two isolated false ozone detections, to 1.22 significance at 61.2 and 1.06$\sigma$ significance at 41.9 km, respectively, where general low-frequency fluctuations in the spectra due to noise or uncertainties in straylight correction were overfit by the retrieval code seeking to find a local minimum in the fit to the spectrum. In Figure A3, by contrast, it is clear to see that the 2.85$\sigma$ detection of ozone at 54.5 km was due to a weak but clearly genuine ozone absorption feature, while the 2.10$\sigma$ detection of ozone at 50.0 km was less certain. These kinds of isolated 2–3$\sigma$ detections were especially common at low altitudes. For this reason, we chose MTDL-2 as the best compromise between having the best possible sensitivity to ozone and filtering out false detections.



21699100, 2023, 5, Downloaded from https://agupubs.onlinelibrary.wiley.com/doi/10.1029/2022JE007697 by Cochrane France, Wiley Online Library on [23/05/2023]. See the Terms and Conditions (https://onlinelibrary.wiley.com/terms-and-conditions) on Wiley Online Library for rules of use; OA articles are governed by the applicable Creative Commons License

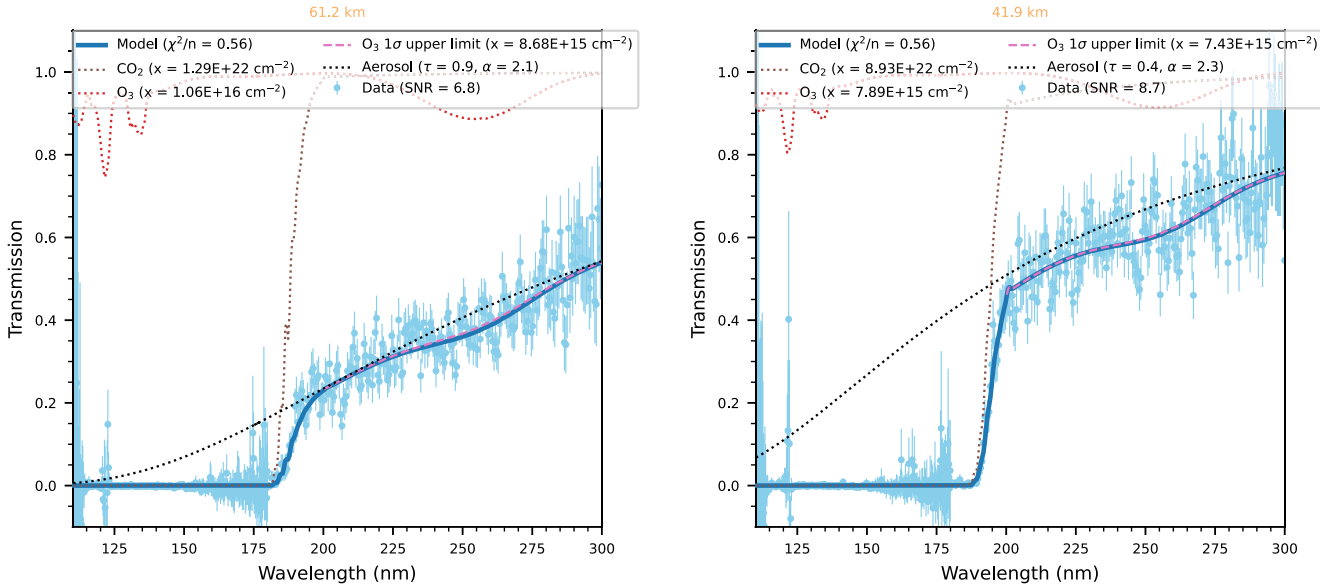



**Figure A2.** Example spectral fits to occultation number 20161118T080220, obtained in orbit 4155 (campaign 11) using star $\delta$Sco, in order to illustrate false 1$\sigma$ detections of ozone. The dark blue lines show the spectral fit to the observed data (light blue scatter plots, with error bars), in contrast to the pink dashed line which shows the same spectral fit with the 1$\sigma$ detection limit of ozone injected into the model. The remaining dotted lines show the relative contribution of the individual gas and aerosol components to the model, together with the retrieved slant abundances given in the legend. In this particular occultation we retrieved a 1.22$\sigma$ detection of ozone at 61.2 km and a 1.06$\sigma$ detection of ozone at 41.9 km. However, both detections were deemed to be false and were due to overfitting of noise in the data.



21699100, 2023, 5, Downloaded from https://agupubs.onlinelibrary.wiley.com/doi/10.1029/2022JE007697 by Cochrane France, Wiley Online Library on [23/05/2023]. See the Terms and Conditions (https://onlinelibrary.wiley.com/terms-and-conditions) on Wiley Online Library for rules of use; OA articles are governed by the applicable Creative Commons License

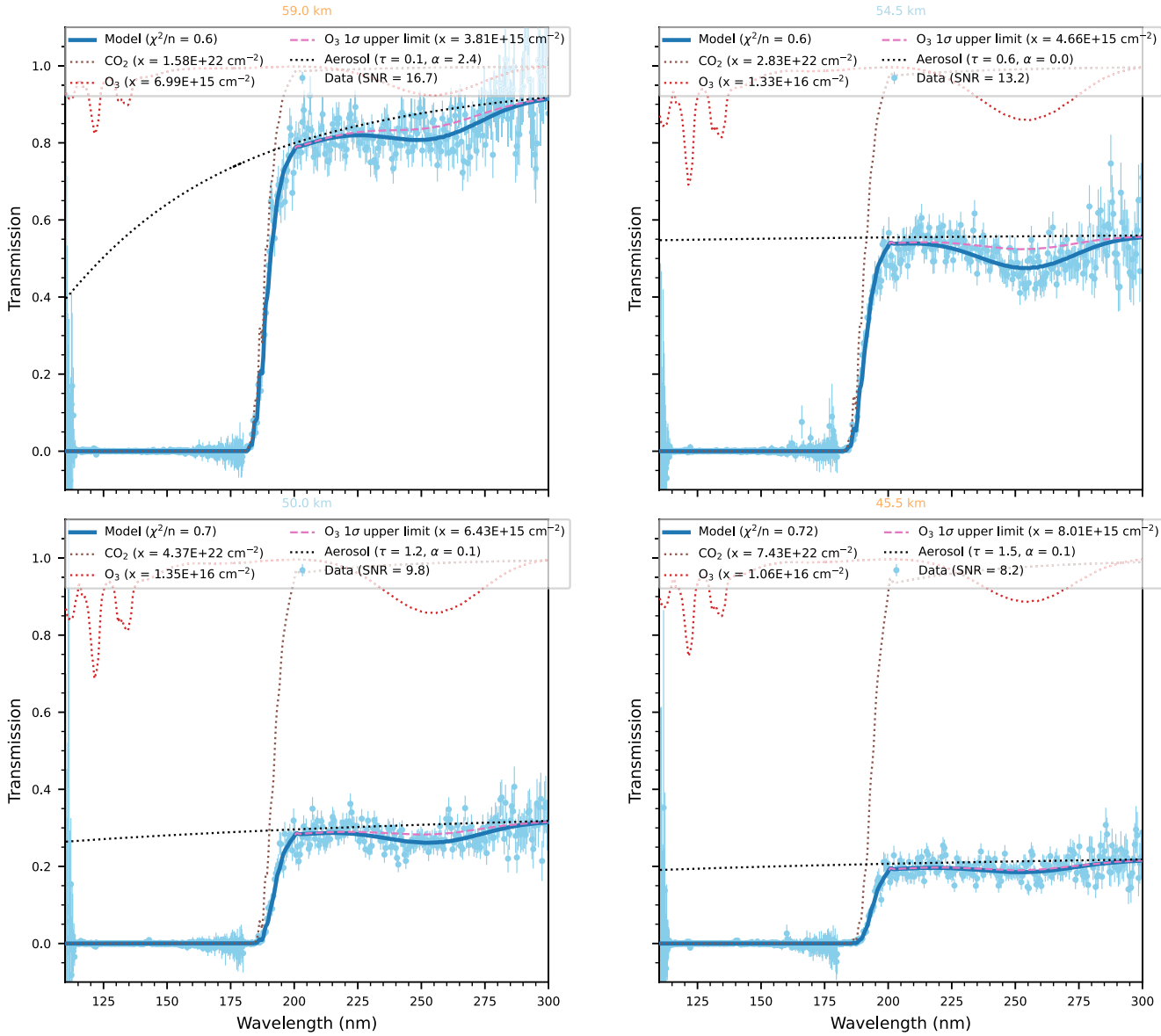



**Figure A3.** Example spectral fits to occultation number 20170615T072357, obtained in orbit 5251 (campaign 15) using star $\alpha^1$Cru. Altitudes in which a detection of ozone of between 1 and 2$\sigma$ significance was retrieved are highlighted using orange titles, while altitudes in which a detection between 2 and 3$\sigma$ significance was retrieved are highlighted using light blue titles. The key to the plots is as in Figure A2. We retrieve a 2.85$\sigma$ detection of ozone at 54.5 km and a 2.10$\sigma$ detection of ozone at 50.0 km. From visual inspection, these two altitudes were deemed to have a genuine presence of ozone.



21699100, 2023, 5, Downloaded from https://agupubs.onlinelibrary.wiley.com/doi/10.1029/2022JE007697 by Cochrane France, Wiley Online Library on [23/05/2023]. See the Terms and Conditions (https://onlinelibrary.wiley.com/terms-and-conditions) on Wiley Online Library for rules of use; OA articles are governed by the applicable Creative Commons License

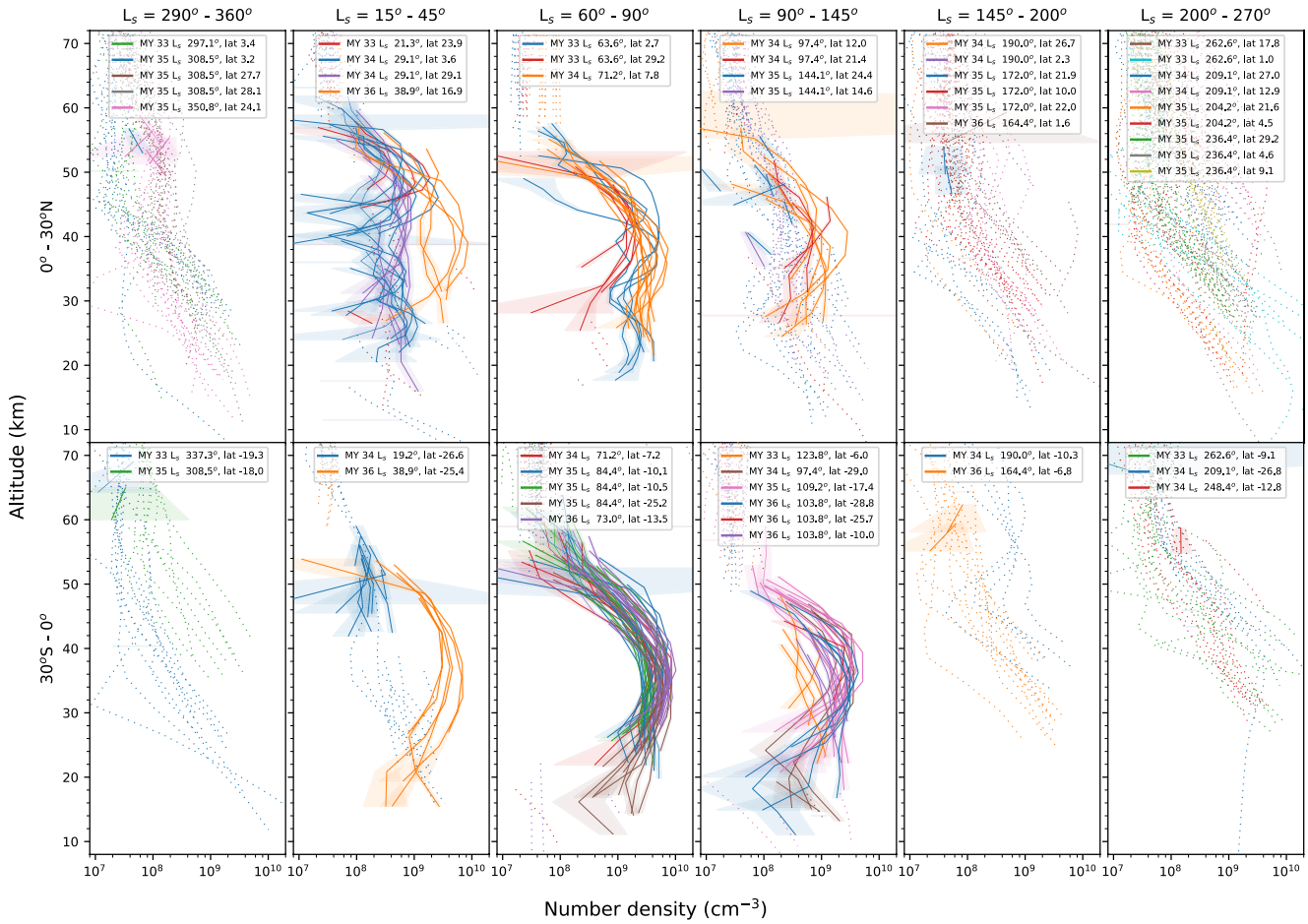



**Figure A4.** Retrieved ozone profiles as in Figure 3, but including detections of ozone of greater than 1$\sigma$ significance into the vertical inversion.

We classified spectra with ozone detections in the 1–2$\sigma$ range as "ambiguous," in that the presence or absence of ozone could not be clearly determined by eye. MTDL-2 therefore only accepted spectra where the genuine presence of ozone could be confirmed beyond much reasonable doubt. As shown in Figure A5, selection using MTDL-1 instead of MTDL-2 would have resulted in numerous false detections at high altitude, particularly in Northern mid-latitudes during the perihelion season. By contrast, only a single false ozone detection was established by MTDL-2 at $L_s$ = 210° (Campaign 22). Nonetheless, the use of MTDL-2 would have also precluded some likely genuine observations of ozone, most notably an ozone layer centered around 45 km altitude that was consistently observed in two sets of occultations south of 55°S at $L_s$ = 20°–30°. These ozone detections lay at the very limits of instrumental sensitivity and were therefore deemed unreliable. In addition, the choice of using MTDL-1 or MTDL-2 could often lead to a change in the retrieved ozone densities close to the edges of the altitude ranges accepted in the vertical inversion, where a more constrained altitude range would result in a reduction in ozone density. In some cases, IUVS is only sensitive to a small number of spectra in a single occultation, and choosing MTDL-2 could result in only one or two ozone column abundance values in close altitudinal proximity to feed into the vertical inversion. This can result in occasional spuriously low ozone local densities that are well below detection limits, which most noticeably affects retrievals of the near-surface layer at high latitudes, as can be clearly seen when contrasting retrievals in the region using MTDL-2 (Figure 5) with using MTDL-1 (Figure A5).



21699100, 2023, 5, Downloaded from https://agupubs.onlinelibrary.wiley.com/doi/10.1029/2022JE007697 by Cochrane France, Wiley Online Library on [23/05/2023]. See the Terms and Conditions (https://onlinelibrary.wiley.com/terms-and-conditions) on Wiley Online Library for rules of use; OA articles are governed by the applicable Creative Commons License

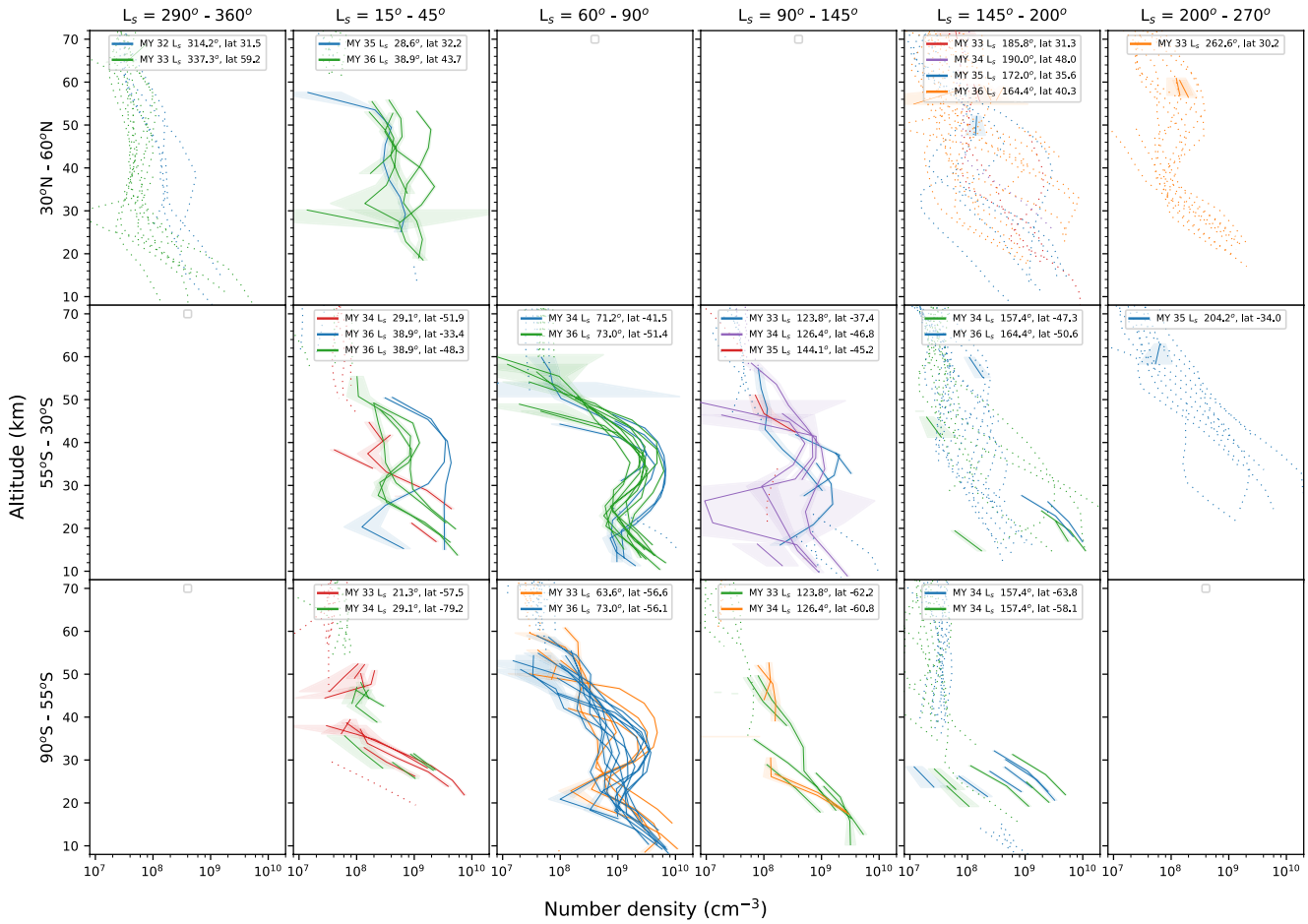



**Figure A5.** Retrieved ozone profiles as in Figure 5, but including detections of ozone of greater than 1$\sigma$ significance into the vertical inversion.

We validated the efficacy of MTDL-2 against the ozone selection methodology of Määttänen et al. (2022a), which we will hereon refer to as the M22 method. Following spectral inversion, we set aside 1,021 individual spectra for a null set, obtained within a solar longitude range of $L_s$ = 240°–280° and a latitude range of 60°S–30°N, where humidity and dust activity was at its peak and where ozone was therefore least likely to be detected. Three statistical criteria were then calculated for each of the spectra in the null set: the percentage a posteriori error on the retrieved ozone slant opacities ($X_{O3}$/err[$X_{O3}$]), the change in goodness of fit to the observed spectra with and without ozone in the forward model ($\chi^2$[no $O_3$]/$\chi^2$[$O_3$]), and the Pearson cross-correlation coefficient between the difference in the fit to the spectra of the model without ozone, and with the difference between the models with and without ozone (Correlation[$O_3$]). The frequency distributions of the three criteria were then fit individually and the 99.87th percentile, equivalent to a 3$\sigma$ detection, calculated for each one, as shown in Figure A6. Any confirmed ozone detection in the full data set therefore had to meet all three criteria from the null set simultaneously, that is to say that $X_{O3}$/err[$X_{O3}$] had to be greater than 3.26, $\chi^2$[no $O_3$]/$\chi^2$[$O_3$] greater than 1.045 and Correlation[$O_3$] greater than 0.333. Due to the size of the null set, only 2–3 null spectra satisfied these constraints individually, and none satisfied all three in combination.



21699100, 2023, 5, Downloaded from https://agupubs.onlinelibrary.wiley.com/doi/10.1029/2022JE007697 by Cochrane France, Wiley Online Library on [23/05/2023]. See the Terms and Conditions (https://onlinelibrary.wiley.com/terms-and-conditions) on Wiley Online Library for rules of use; OA articles are governed by the applicable Creative Commons License

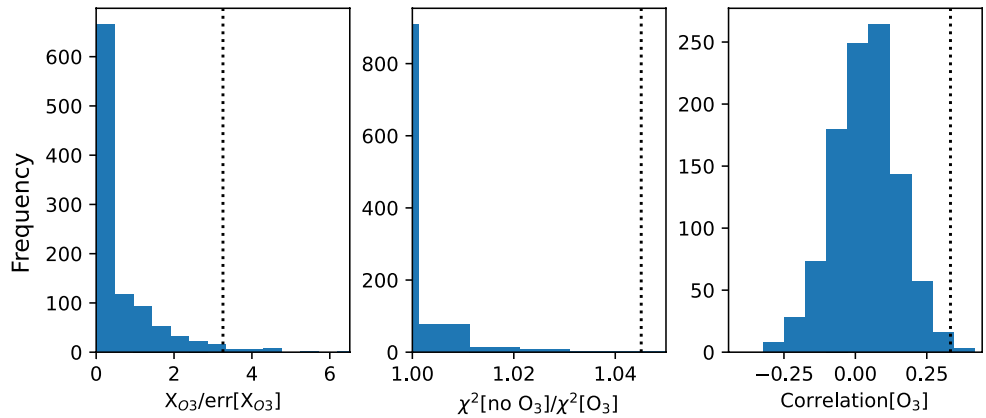



**Figure A6.** Frequency distribution of null test spectra as a function of three selection criteria defined in M22: (left) a posteriori error on the retrieved ozone slant density, (center) difference in fit to the observed spectrum with and without ozone in the forward model, (right) Pearson cross-correlation coefficient. Vertical black dotted lines indicate 3$\sigma$ (99.87th percentile) value selection thresholds for each of the criteria.

In Figure A7 we plot the frequency distributions of individual ozone detections that were not classified in the same way by the MTDL-1, MTDL-2, and M22 methods in combination. The vast majority of spectra selected by M22 but rejected by MTDL-2 were classified as ambiguous by MTDL, and were therefore accepted in MTDL-1. In total around 46% of all ambiguous spectra were classified as confirmed ozone detections by M22, while only 8 out of the 20,756 total spectra rejected by MTDL-1 were classified as detections by M22, and only 14 out of a total of 1,742 spectra classified as detections by MTDL-2 were rejected by M22. We therefore show that, for a large null set, M22 and MTDL could be seen to give approximately equivalent results, but MTDL could be used for small data sets from which an adequate null set could not be compiled.

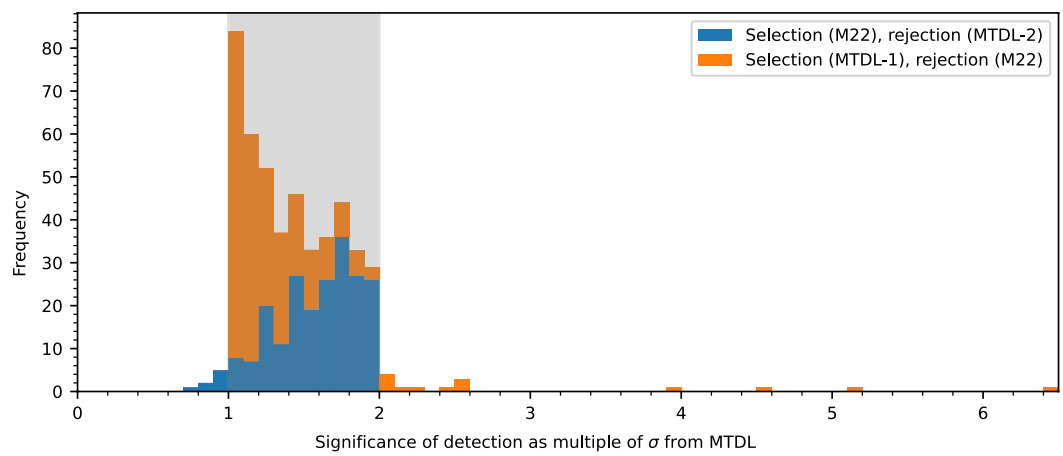



**Figure A7.** Frequency distribution of spectra which were taken as confirmed ozone detections by M22 but rejected by MTDL (in blue), or vice versa (in orange), as a function of the significance of ozone detection derived using MTDL. The gray region encompasses "ambiguous" spectra that were accepted as ozone detections by MTDL-1 but rejected by MTDL-2. A single 20$\sigma$ outlier rejected by M22 but accepted by MTDL was excluded from the plot for clarity.

## Conflict of Interest

The authors declare no conflicts of interest relevant to this study.



21699100, 2023, 5, Downloaded from https://agupubs.onlinelibrary.wiley.com/doi/10.1029/2022JE007697 by Cochrane France, Wiley Online Library on [23/05/2023]. See the Terms and Conditions (https://onlinelibrary.wiley.com/terms-and-conditions) on Wiley Online Library for rules of use; OA articles are governed by the applicable Creative Commons License

## Data Availability Statement

This analysis makes use of the MAVEN/IUVS processed (level 1C) stellar occultation data (Schneider, 2022), which can be freely downloaded in FITS format from the NASA Planetary Data System (PDS), identified by "occultation" with version/revision tag v13_r01. It is also publicly available on the LASP MAVEN Science Data Center (SDC, https://lasp.colorado.edu/maven/sdc/public/). The output data from this study, including the results of both the spectral and vertical retrievals of ozone from the 583 selected stellar occultations, together with the associated model output from the Planetary Climate Model (PCM), can be downloaded from the CU Scholar Data Repository (Braude et al., 2022). The SPICAM data used in this study was obtained from the ESPRI/IPSL repository (Määttänen et al., 2022b).

**Acknowledgments**
This work was supported by funding from the MAVEN mission as part of NASA's Mars Exploration Program. The MAVEN mission is supported by NASA in association with the University of Colorado and NASA's Goddard Space Flight Center. ASB, FM, FL, AM, LV, and ZF acknowledge funding from the Centre National d'Études Spatiales (CNES) via the French National Centre for Scientific Research (CNRS).

## References

Atwood, S. A., Smith, M. D., Badri, K., Edwards, C. S., Christensen, P. R., Wolff, M. J., et al. (2022). Diurnal variability in EMIRS daytime observations of water ice clouds during Mars aphelion-season. *Geophysical Research Letters*, *49*(15), e99654. https://doi.org/10.1029/2022GL099654

Banfield, D., Conrath, B. J., Smith, M. D., Christensen, P. R., & Wilson, R. J. (2003). Forced waves in the Martian atmosphere from MGS TES nadir data. *Icarus*, *161*(2), 319–345. https://doi.org/10.1016/S0019-1035(02)00044-1

Barnes, J. R., Pollack, J. B., Haberle, R. M., Leovy, C. B., Zurek, R. W., Lee, H., & Schaeffer, J. (1993). Mars atmospheric dynamics as simulated by the NASA Ames general circulation model. 2. Transient baroclinic eddies. *Journal of Geophysical Research*, *98*(E2), 3125–3148. https://doi.org/10.1029/92JE02935

Barth, C. A., & Hord, C. W. (1971). Mariner ultraviolet spectrometer: Topography and polar cap. *Science*, *173*(3993), 197–201. https://doi.org/10.1126/science.173.3993.197

Barth, C. A., Hord, C. W., Stewart, A. I., Lane, A. L., Dick, M. L., & Anderson, G. P. (1973). Mariner 9 ultraviolet spectrometer experiment: Seasonal variation of ozone on Mars. *Science*, *179*(4075), 795–796. https://doi.org/10.1126/science.179.4075.795

Battalio, M., Szunyogh, I., & Lemmon, M. (2018). Wave energetics of the southern hemisphere of Mars. *Icarus*, *309*, 220–240. https://doi.org/10.1016/j.icarus.2018.03.015

Blamont, J. E., & Chassefiere, E. (1993). First detection of ozone in the middle atmosphere of Mars from solar occultation measurements. *Icarus*, *104*(2), 324–336. https://doi.org/10.1006/icar.1993.1104

Blamont, J. E., Chassefiere, E., Goutail, J. P., Mege, B., Nunes-Pinharanda, M., Souchon, G., et al. (1989). Vertical profiles of dust and ozone in the Martian atmosphere deduced from solar occultation measurements. *Nature*, *341*(6243), 600–603. https://doi.org/10.1038/341600a0

Braude, A. S., Gupta, S., & Schneider, N. M. (2022). Ozone vertical profiles from MAVEN/IUVS nightside stellar occultations [Dataset]. University of Colorado Boulder. https://doi.org/10.25810/6yrq-yp38

Brown, M. A. J., Patel, M. R., Lewis, S. R., Holmes, J. A., Sellers, G. J., Streeter, P. M., et al. (2022). Impacts of heterogeneous chemistry on vertical profiles of Martian ozone. *Journal of Geophysical Research: Planets*, *127*(11), e2022JE007346. https://doi.org/10.1029/2022JE007346

Chaffin, M. S., Chaufray, J. Y., Deighan, J., Schneider, N. M., McClintock, W. E., Stewart, A. I. F., et al. (2015). Three-dimensional structure in the Mars H corona revealed by IUVS on MAVEN. *Geophysical Research Letters*, *42*(21), 9001–9008. https://doi.org/10.1002/2015GL065287

Clancy, R. T., Grossman, A. W., Wolff, M. J., James, P. B., Rudy, D. J., Billawala, Y. N., et al. (1996). Water vapor saturation at low altitudes around Mars aphelion: A key to Mars climate? *Icarus*, *122*(1), 36–62. https://doi.org/10.1006/icar.1996.0108

Clancy, R. T., & Nair, H. (1996). Annual (perihelion-aphelion) cycles in the photochemical behavior of the global Mars atmosphere. *Journal of Geophysical Research*, *101*(E5), 12785–12790. https://doi.org/10.1029/96JE00836

Clancy, R. T., Sandor, B., & Moriarty-Schieven, G. (2004). A measurement of the 362 GHz absorption line of Mars atmospheric $H_2O_2$. *Icarus*, *168*(1), 116–121. https://doi.org/10.1016/j.icarus.2003.12.003

Clancy, R. T., Wolff, M. J., & James, P. B. (1999). Minimal aerosol loading and global increases in atmospheric ozone during the 1996–1997 Martian northern spring season. *Icarus*, *138*(1), 49–63. https://doi.org/10.1006/icar.1998.6059

Clancy, R. T., Wolff, M. J., Lefèvre, F., Cantor, B. A., Malin, M. C., & Smith, M. D. (2016). Daily global mapping of Mars ozone column abundances with MARCI UV band imaging. *Icarus*, *266*, 112–133. https://doi.org/10.1016/j.icarus.2015.11.016

Clarke, J. T., Mayyasi, M., Bhattacharyya, D., Schneider, N. M., McClintock, W. E., Deighan, J. I., et al. (2017). Variability of D and H in the Martian upper atmosphere observed with the MAVEN IUVS echelle channel. *Journal of Geophysical Research: Space Physics*, *122*(2), 2336–2344. https://doi.org/10.1002/2016JA023479

Daerden, F., Neary, L., Viscardy, S., García Muñoz, A., Clancy, R. T., Smith, M. D., et al. (2019). Mars atmospheric chemistry simulations with the GEM-Mars general circulation model. *Icarus*, *326*, 197–224. https://doi.org/10.1016/j.icarus.2019.02.030

Daerden, F., Neary, L., Wolff, M. J., Clancy, R. T., Lefèvre, F., Whiteway, J. A., et al. (2022). Planet-wide ozone destruction in the middle atmosphere on Mars during global dust storm. *Geophysical Research Letters*, *49*(11), e2022GL098821. https://doi.org/10.1029/2022GL098821

Dubovik, O., Smirnov, A., Holben, B. N., King, M. D., Kaufman, Y. J., Eck, T. F., & Slutsker, I. (2000). Accuracy assessments of aerosol optical properties retrieved from Aerosol Robotic Network (AERONET) Sun and sky radiance measurements. *Journal of Geophysical Research*, *105*(D8), 9791–9806. https://doi.org/10.1029/2000JD900040

Encrenaz, T., Bézard, B., Greathouse, T. K., Richter, M. J., Lacy, J. H., Atreya, S. K., et al. (2004). Hydrogen peroxide on Mars: Evidence for spatial and seasonal variations. *Icarus*, *170*(2), 424–429. https://doi.org/10.1016/j.icarus.2004.05.008

Fast, K. E., Kostiuk, T., Espenak, F., Annen, J., Buhl, D., Hewagama, T., et al. (2006). Ozone abundance on Mars from infrared heterodyne spectra. I. Acquisition, retrieval, and anticorrelation with water vapor. *Icarus*, *181*(2), 419–431. https://doi.org/10.1016/j.icarus.2005.12.001

Fast, K. E., Kostiuk, T., Lefèvre, F., Hewagama, T., Livengood, T. A., Delgado, J. D., et al. (2009). Comparison of HIPWAC and Mars Express SPICAM observations of ozone on Mars 2006–2008 and variation from 1993 IRHS observations. *Icarus*, *203*(1), 20–27. https://doi.org/10.1016/j.icarus.2009.05.005

Fukuhara, T., & Imamura, T. (2005). Waves encircling the summer southern pole of Mars observed by MGS TES. *Geophysical Research Letters*, *32*(18), L18811. https://doi.org/10.1029/2005GL023819

Gröller, H., Montmessin, F., Yelle, R. V., Lefèvre, F., Forget, F., Schneider, N. M., et al. (2018). MAVEN/IUVS stellar occultation measurements of Mars atmospheric structure and composition. *Journal of Geophysical Research: Planets*, *123*(6), 1449–1483. https://doi.org/10.1029/2017JE005466



21699100, 2023, 5, Downloaded from https://agupubs.onlinelibrary.wiley.com/doi/10.1029/2022JE007697 by Cochrane France, Wiley Online Library on [23/05/2023]. See the Terms and Conditions (https://onlinelibrary.wiley.com/terms-and-conditions) on Wiley Online Library for rules of use; OA articles are governed by the applicable Creative Commons License

Gröller, H., Yelle, R. V., Koskinen, T. T., Montmessin, F., Lacombe, G., Schneider, N. M., et al. (2015). Probing the Martian atmosphere with MAVEN/IUVS stellar occultations. *Geophysical Research Letters*, *42*(21), 9064–9070. https://doi.org/10.1002/2015GL065294

Guha, B. K., Panda, J., Newman, C. E., & Richardson, M. I. (2021). Dust and water ice variability and their interaction pattern during Martian low-dust and high-dust periods. *Planetary and Space Science*, *209*, 105357. https://doi.org/10.1016/j.pss.2021.105357

Gupta, S., Yelle, R. V., Schneider, N. M., Jain, S. K., González-Galindo, F., Verdier, L., et al. (2022). Thermal structure of the Martian upper mesosphere/lower thermosphere from MAVEN/IUVS stellar occultations. *Journal of Geophysical Research: Planets*, *127*(11), e2022JE007534. https://doi.org/10.1029/2022JE007534

Guslyakova, S., Fedorova, A., Lefèvre, F., Korablev, O., Montmessin, F., Trokhimovskiy, A., & Bertaux, J. L. (2016). Long-term nadir observations of the $O_2$ dayglow by SPICAM IR. *Planetary and Space Science*, *122*, 1–12. https://doi.org/10.1016/j.pss.2015.12.006

Guzewich, S. D., Talaat, E. R., & Waugh, D. W. (2012). Observations of planetary waves and nonmigrating tides by the Mars Climate Sounder. *Journal of Geophysical Research*, *117*(E3), E03010. https://doi.org/10.1029/2011JE003924

Hinson, D. P. (2006). Radio occultation measurements of transient eddies in the northern hemisphere of Mars. *Journal of Geophysical Research*, *111*(E5), E05002. https://doi.org/10.1029/2005JE002612

Hinson, D. P., Wilson, R. J., Smith, M. D., & Conrath, B. J. (2003). Stationary planetary waves in the atmosphere of Mars during southern winter. *Journal of Geophysical Research*, *108*(E1), 5004. https://doi.org/10.1029/2002JE001949

Holmes, J. A., Lewis, S. R., & Patel, M. R. (2017). On the link between Martian total ozone and potential vorticity. *Icarus*, *282*, 104–117. https://doi.org/10.1016/j.icarus.2016.10.004

Jain, S. K., Stewart, A. I. F., Schneider, N. M., Deighan, J., Stiepen, A., Evans, J. S., et al. (2015). The structure and variability of Mars upper atmosphere as seen in MAVEN/IUVS dayglow observations. *Geophysical Research Letters*, *42*(21), 9023–9030. https://doi.org/10.1002/2015GL065419

Jakosky, B. M., Lin, R. P., Grebowsky, J. M., Luhmann, J. G., Mitchell, D. F., Beutelschies, G., et al. (2015). The Mars atmosphere and volatile evolution (MAVEN) mission. *Space Science Reviews*, *195*(1–4), 3–48. https://doi.org/10.1007/s11214-015-0139-x

Jones, A. R., Wolff, M., Alshamsi, M., Osterloo, M., Bay, P., Brennan, N., et al. (2021). The Emirates Exploration Imager (EXI) instrument on the Emirates Mars mission (EMM) hope mission. *Space Science Reviews*, *217*(8), 81. https://doi.org/10.1007/s11214-021-00852-5

Khayat, A. S. J., Smith, M. D., Wolff, M., Daerden, F., Neary, L., Patel, M. R., et al. (2021). ExoMars TGO/NOMAD-UVIS vertical profiles of ozone: 2. The high-altitude layers of atmospheric ozone. *Journal of Geophysical Research: Planets*, *126*(11), e2021JE006834. https://doi.org/10.1029/2021JE006834

Korablev, O. I., Montmessin, F., Trokhimovskiy, A., Fedorova, A. A., Shakun, A. V., Grigoriev, A. V., et al. (2018). The Atmospheric Chemistry Suite (ACS) of three spectrometers for the ExoMars 2016 Trace gas orbiter. *Space Science Reviews*, *214*(1), 7. https://doi.org/10.1007/s11214-017-0437-6

Krasnopolsky, V. A., & Parshev, V. A. (1979). Ozone and photochemistry of the martian lower atmosphere. *Planetary and Space Science*, *27*(2), 113–120. https://doi.org/10.1016/0032-0633(79)90040-0

Lebonnois, S., Quémerais, E., Montmessin, F., Lefèvre, F., Perrier, S., Bertaux, J.-L., & Forget, F. (2006). Vertical distribution of ozone on Mars as measured by SPICAM/Mars Express using stellar occultations. *Journal of Geophysical Research*, *111*(E9), E09S05. https://doi.org/10.1029/2005JE002643

Lefèvre, F., Bertaux, J.-L., Clancy, R. T., Encrenaz, T., Fast, K., Forget, F., et al. (2008). Heterogeneous chemistry in the atmosphere of Mars. *Nature*, *454*(7207), 971–975. https://doi.org/10.1038/nature07116

Lefèvre, F., & Krasnopolsky, V. (2017). Atmospheric photochemistry. In R. M. Haberle, R. T. Clancy, F. Forget, M. D. Smith, & R. W. Zurek (Eds.), *The atmosphere and climate of Mars* (pp. 374–404). https://doi.org/10.1017/9781139060172.013

Lefèvre, F., Lebonnois, S., Montmessin, F., & Forget, F. (2004). Three-dimensional modeling of ozone on Mars. *Journal of Geophysical Research*, *109*(E7), E07004. https://doi.org/10.1029/2004JE002268

Lefèvre, F., Montmessin, F., Schneider, N. M., Deighan, J., Jain, S., Stewart, I. F., et al. (2015). Mars Ozone mapping with MAVEN IUVS. In *AGU fall meeting abstracts* (Vol. 2015, p. P21A-2065).

Lefèvre, F., Trokhimovskiy, A., Fedorova, A., Baggio, L., Lacombe, G., Määttänen, A., et al. (2021). Relationship between the ozone and water vapor columns on Mars as observed by SPICAM and calculated by a global climate model. *Journal of Geophysical Research: Planets*, *126*(4), e2021JE006838. https://doi.org/10.1029/2021JE006838

Lewis, S. R., Mulholland, D. P., Read, P. L., Montabone, L., Wilson, R. J., & Smith, M. D. (2016). The solsticial pause on Mars: 1. A planetary wave reanalysis. *Icarus*, *264*, 456–464. https://doi.org/10.1016/j.icarus.2015.08.039

Määttänen, A., Lefèvre, F., Verdier, L., Montmessin, F., Listowski, C., Guilbon, S., et al. (2022a). Ozone vertical distribution in Mars years 27–30 from SPICAM/MEX UV occultations. *Icarus*, *387*, 115162. https://doi.org/10.1016/j.icarus.2022.115162

Määttänen, A., Verdier, L., Lefèvre, F., Montmessin, F., Listowski, C., Guilbon, S., et al. (2022b). Ozone vertical distribution in Mars years 27–30 from SPICAM/MEX UV occultations [Dataset]. ESPRI/IPSL, *387*, 115162. https://doi.org/10.14768/C155973B-C810-4917-B98E-F4D905ED4FC1

Markwardt, C. (2009). Non-linear least squares fitting in IDL with MPFIT. In D. A. Bohlender, D. Durand, & P. Dowler (Eds.), *Astronomical data analysis software and systems xviii asp conference series* (Vol. 411, p. 251). Astronomical Society of the Pacific. Retrieved from https://arxiv.org/abs/0902.2850

McCleese, D. J., Heavens, N. G., Schofield, J. T., Abdou, W. A., Bandfield, J. L., Calcutt, S. B., et al. (2010). Structure and dynamics of the Martian lower and middle atmosphere as observed by the Mars Climate Sounder: Seasonal variations in zonal mean temperature, dust, and water ice aerosols. *Journal of Geophysical Research*, *115*(E12), E12016. https://doi.org/10.1029/2010JE003677

McClintock, W. E., Schneider, N. M., Holsclaw, G. M., Clarke, J. T., Hoskins, A. C., Stewart, I., et al. (2015). The imaging ultraviolet spectrograph (IUVS) for the MAVEN mission. *Space Science Reviews*, *195*(1–4), 75–124. https://doi.org/10.1007/s11214-014-0098-7

McElroy, M. B., & Donahue, T. M. (1972). Stability of the martian atmosphere. *Science*, *177*(4053), 986–988. https://doi.org/10.1126/science.177.4053.986

Medvedev, A. S., Nakagawa, H., Mockel, C., Yiğit, E., Kuroda, T., Hartogh, P., et al. (2016). Comparison of the Martian thermospheric density and temperature from IUVS/MAVEN data and general circulation modeling. *Geophysical Research Letters*, *43*(7), 3095–3104. https://doi.org/10.1002/2016GL068388

Mitchell, D. M., Montabone, L., Thomson, S., & Read, P. L. (2015). Polar vortices on Earth and Mars: A comparative study of the climatology and variability from reanalyses. *Quarterly Journal of the Royal Meteorological Society*, *141*(687), 550–562. https://doi.org/10.1002/qj.2376

Montabone, L., Forget, F., Millour, E., Wilson, R. J., Lewis, S. R., Cantor, B., et al. (2015). Eight-year climatology of dust optical depth on Mars. *Icarus*, *251*, 65–95. https://doi.org/10.1016/j.icarus.2014.12.034



21699100, 2023, 5, Downloaded from https://agupubs.onlinelibrary.wiley.com/doi/10.1029/2022JE007697 by Cochrane France, Wiley Online Library on [23/05/2023]. See the Terms and Conditions (https://onlinelibrary.wiley.com/terms-and-conditions) on Wiley Online Library for rules of use; OA articles are governed by the applicable Creative Commons License

Montabone, L., Spiga, A., Kass, D. M., Kleinböhl, A., Forget, F., & Millour, E. (2020). Martian year 34 column dust climatology from Mars climate sounder observations: Reconstructed maps and model simulations. *Journal of Geophysical Research: Planets*, *125*(8), e2019JE006111. https://doi.org/10.1029/2019JE006111

Montmessin, F., Forget, F., Rannou, P., Cabane, M., & Haberle, R. M. (2004). Origin and role of water ice clouds in the Martian water cycle as inferred from a general circulation model. *Journal of Geophysical Research*, *109*(E10), E10004. https://doi.org/10.1029/2004JE002284

Montmessin, F., & Lefèvre, F. (2013). Transport-driven formation of a polar ozone layer on Mars. *Nature Geoscience*, *6*(11), 930–933. https://doi.org/10.1038/ngeo1957

Montmessin, F., Quémerais, E., Bertaux, J. L., Korablev, O., Rannou, P., & Lebonnois, S. (2006). Stellar occultations at UV wavelengths by the SPICAM instrument: Retrieval and analysis of Martian haze profiles. *Journal of Geophysical Research*, *111*(E9), E09S09. https://doi.org/10.1029/2005JE002662

Montmessin, F., Smith, M. D., Langevin, Y., Mellon, M. T., & Fedorova, A. (2017). The water cycle. In R. M. Haberle, R. T. Clancy, F. Forget, M. D. Smith, & R. W. Zurek (Eds.), *The atmosphere and climate of Mars* (pp. 295–337). https://doi.org/10.1017/9781139060172.011

Mulholland, D. P., Lewis, S. R., Read, P. L., Madeleine, J.-B., & Forget, F. (2016). The solsticial pause on Mars: 2. Modelling and investigation of causes. *Icarus*, *264*, 465–477. https://doi.org/10.1016/j.icarus.2015.08.038

Olsen, K. S., Fedorova, A. A., Trokhimovskiy, A., Montmessin, F., Lefèvre, F., Korablev, O., et al. (2022). Seasonal changes in the vertical structure of ozone in the Martian lower atmosphere and its relationship to water vapour. *Journal of Geophysical Research: Planets*, *127*(10), e2022JE007213. https://doi.org/10.1029/2022JE007213

Olsen, K. S., Lefèvre, F., Montmessin, F., Fedorova, A. A., Trokhimovskiy, A., Baggio, L., et al. (2021). The vertical structure of CO in the Martian atmosphere from the ExoMars Trace gas orbiter. *Nature Geoscience*, *14*(2), 67–71. https://doi.org/10.1038/s41561-020-00678-w

Olsen, K. S., Lefèvre, F., Montmessin, F., Trokhimovskiy, A., Baggio, L., Fedorova, A., et al. (2020). First detection of ozone in the mid-infrared at Mars: Implications for methane detection. *Astronomy & Astrophysics*, *639*, A141. https://doi.org/10.1051/0004-6361/202038125

O'Neill, N., & Royer, A. (1993). Extraction of bimodal aerosol-size distribution radii from spectral and angular slope (Angstrom) coefficients. *Applied Optics*, *32*(9), 1642–1645. https://doi.org/10.1364/AO.32.001642

Parkinson, T. D., & Hunten, D. M. (1972). Spectroscopy and aeronomy of $O_2$ on Mars. *Journal of the Atmospheric Sciences*, *29*(7), 1380–1390. https://doi.org/10.1175/1520-0469(1972)029⟨1380:SAAOOO⟩2.0.CO;2

Patel, M. R., Sellers, G., Mason, J. P., Holmes, J. A., Brown, M. A. J., Lewis, S. R., et al. (2021). ExoMars TGO/NOMAD-UVIS vertical profiles of ozone: 1. Seasonal variation and comparison to water. *Journal of Geophysical Research: Planets*, *126*(11), e2021JE006837. https://doi.org/10.1029/2021JE006837

Perrier, S., Bertaux, J. L., Lefèvre, F., Lebonnois, S., Korablev, O., Fedorova, A., & Montmessin, F. (2006). Global distribution of total ozone on Mars from SPICAM/MEX UV measurements. *Journal of Geophysical Research*, *111*(E9), E09S06. https://doi.org/10.1029/2006JE002681

Piccialli, A., Vandaele, A. C., Willame, Y., Määttänen, A., Trompet, L., Erwin, J. T., et al. (2023). Martian ozone observed by TGO/NOMAD-UVIS solar occultation: An inter-comparison of three retrieval methods. *Earth and Space Science*, *10*(2), e2022EA002429. https://doi.org/10.1029/2022EA002429

Putzig, N. E., & Mellon, M. T. (2007). Apparent thermal inertia and the surface heterogeneity of Mars. *Icarus*, *191*(1), 68–94. https://doi.org/10.1016/j.icarus.2007.05.013

Quémerais, E., Bertaux, J.-L., Korablev, O., Dimarellis, E., Cot, C., Sandel, B. R., & Fussen, D. (2006). Stellar occultations observed by SPICAM on Mars Express. *Journal of Geophysical Research*, *111*(E9), E09S04. https://doi.org/10.1029/2005JE002604

Schneider, N. (2022). MAVEN IUVS calibrated-level data product bundle [Dataset]. NASA Planetary Data System. https://doi.org/10.17189/1518946

Smith, M. D. (2004). Interannual variability in TES atmospheric observations of Mars during 1999–2003. *Icarus*, *167*(1), 148–165. https://doi.org/10.1016/j.icarus.2003.09.010

Smith, M. D., Badri, K., Atwood, S. A., Edwards, C. S., Christensen, P. R., Wolff, M. J., et al. (2022). EMIRS observations of the aphelion-season Mars atmosphere. *Geophysical Research Letters*, *49*(15), e2022GL099636. https://doi.org/10.1029/2022GL099636

Teanby, N. A., Irwin, P. G. J., de Kok, R., Jolly, A., Bézard, B., Nixon, C. A., & Calcutt, S. B. (2009). Titan's stratospheric $C_2N_2$, $C_3H_4$, and $C_4H_2$ abundances from Cassini/CIRS far-infrared spectra. *Icarus*, *202*, 620–631. https://doi.org/10.1016/j.icarus.2009.03.022

Teanby, N. A., Irwin, P. G. J., & Moses, J. I. (2019). Neptune's carbon monoxide profile and phosphine upper limits from Herschel/SPIRE: Implications for interior structure and formation. *Icarus*, *319*, 86–98. https://doi.org/10.1016/j.icarus.2018.09.014

Trompet, L., Robert, S., Mahieux, A., Schmidt, F., Erwin, J., & Vandaele, A. C. (2021). Phosphine in Venus' atmosphere: Detection attempts and upper limits above the cloud top assessed from the SOIR/VEx spectra. *Astronomy & Astrophysics*, *645*, L4. https://doi.org/10.1051/0004-6361/202039932

Vago, J., Witasse, O., Svedhem, H., Baglioni, P., Haldemann, A., Gianfiglio, G., et al. (2015). ESA ExoMars program: The next step in exploring Mars. *Solar System Research*, *49*(7), 518–528. https://doi.org/10.1134/S0038094615070199

Vandaele, A. C., Lopez-Moreno, J. J., Patel, M. R., Bellucci, G., Daerden, F., Ristic, B., et al. (2018). NOMAD, an integrated suite of three spectrometers for the ExoMars Trace gas mission: Technical description, science objectives and expected performance. *Space Science Reviews*, *214*(5), 80. https://doi.org/10.1007/s11214-018-0517-2

Waugh, D. W., Toigo, A. D., Guzewich, S. D., Greybush, S. J., Wilson, R. J., & Montabone, L. (2016). Martian polar vortices: Comparison of reanalyses. *Journal of Geophysical Research: Planets*, *121*(9), 1770–1785. https://doi.org/10.1002/2016JE005093

Willame, Y., Vandaele, A. C., Depiesse, C., Lefèvre, F., Letocart, V., Gillotay, D., & Montmessin, F. (2017). Retrieving cloud, dust and ozone abundances in the Martian atmosphere using SPICAM/UV nadir spectra. *Planetary and Space Science*, *142*, 9–25. https://doi.org/10.1016/j.pss.2017.04.011

Wilson, R. J., Banfield, D., Conrath, B. J., & Smith, M. D. (2002). Traveling waves in the northern hemisphere of Mars. *Geophysical Research Letters*, *29*(14), 1684–29-4. https://doi.org/10.1029/2002GL014866

Wolff, M. J., Fernando, A., Smith, M. D., Forget, F., Millour, E., Atwood, S. A., et al. (2022). Diurnal variations in the aphelion cloud Belt as observed by the Emirates Exploration Imager (EXI). *Geophysical Research Letters*, *49*(18), e2022GL100477. https://doi.org/10.1029/2022GL100477



21699100, 2023, 5, Downloaded from https://agupubs.onlinelibrary.wiley.com/doi/10.1029/2022JE007697 by Cochrane France, Wiley Online Library on [23/05/2023]. See the Terms and Conditions (https://onlinelibrary.wiley.com/terms-and-conditions) on Wiley Online Library for rules of use; OA articles are governed by the applicable Creative Commons License